Dark energy survey year 3 results: Cosmological constraints from cluster abundances, weak lensing, and galaxy clustering

T. M. C. Abbott, M. Aguena, A. Alarcon, A. Amon, D. Anbajagane, F. Andrade-Oliveira, S. Avila, S. S. Allam, D. Bacon, M. R. Becker, S. Bhargava, J. Blazek, S. Bocquet, D. Brooks, A. Carnero Rosell, A. Carretero, E. J. Castander, C. Chang, A. Choi, C. Conselice, M. Costanzi, A. Carnero Rosell, Carretero, D. M. Costanzi, A. Crocce, C. L. N. da Costa, M. E. S. Pereira, C. Doux, A. Choi, B. C. Conselice, M. Costanzi, C. Dodelson, C. Chang, D. L. N. da Costa, A. Esteves, S. Everett, C. Doux, D. L. N. Davis, S. Desai, H. T. Diehl, S. Dodelson, Carria, P. Doel, J. J. Elvin-Poole, S. Grandis, D. Gruen, R. A. Gruendl, G. Gutierrez, J. García-Bellido, M. Gatti, G. Giannini, L. P. Giles, S. Grandis, D. Gruen, L. A. Gruendl, G. Gutierrez, L. Harrison, S. R. Hinton, C. L. Hollowood, G. K. Honscheid, Al. N. Jeffrey, L. J. J. Hocullough, D. L. Hollowood, D. L. Hollowood, M. Lima, L. L. Marshall, L. Marshall, J. McCullough, M. J. Mena-Fern'andez, R. Miquel, M. Lima, Al. H. Lin, L. J. J. Mohr, Al. R. Walker, M. Paterno, A. A. Plazas Malagón, Malagón, A. Rorredon, A. Roodman, L. Rozo, E. S. Rykoff, M. R. Rosenfeld, N. Weaverdyck, Chang, R. L. C. Dando, M. A. Troxel, A. R. Walker, David H. Weinberg, M. Weaverdyck, S. R. H. Wechsler, C. S. Shang, L. Weller, R. L. Y. Wu, M. Yamamoto, So. B. Yanny, Y. Zhang, and C. Zhou G. Zhou

(DES Collaboration)*

```
<sup>1</sup>Cerro Tololo Inter-American Observatory, NSF's National Optical-Infrared Astronomy Research
                                Laboratory, Casilla 603, La Serena, Chile
 <sup>2</sup>Laboratório Interinstitucional de e-Astronomia—LIneA, Av. Pastor Martin Luther King Jr, 126 Del
            Castilho, Nova América Offices, Torre 3000/sala 817 CEP: 20765-000, Brazil
           <sup>3</sup>Institute of Space Sciences (ICE, CSIC), Campus UAB, Carrer de Can Magrans,
                                        s/n, 08193 Barcelona, Spain
   <sup>4</sup>Kavli Institute for Cosmological Physics, University of Chicago, Chicago, Illinois 60637, USA
     <sup>5</sup>Physik-Institut, University of Zürich, Winterthurerstrasse 190, CH-8057 Zürich, Switzerland
<sup>6</sup>Centro de Investigaciones Energéticas, Medioambientales y Tecnológicas (CIEMAT), Madrid, Spain
                   <sup>I</sup>Institute of Cosmology and Gravitation, University of Portsmouth,
                                 Portsmouth, PO1 3FX, United Kingdom
        <sup>8</sup>Argonne National Laboratory, 9700 South Cass Avenue, Lemont, Illinois 60439, USA
            Department of Physics and Astronomy, Pevensey Building, University of Sussex,
                                  Brighton, BN1 9QH, United Kingdom
         <sup>10</sup>Department of Physics, Northeastern University, Boston, Massachusetts 02115, USA
              <sup>1</sup>University Observatory, Faculty of Physics, Ludwig-Maximilians-Universität,
                                 Scheinerstr. 1, 81679 Munich, Germany
                  <sup>12</sup>Department of Physics and Astronomy, University College London,
                           Gower Street, London, WC1E 6BT, United Kingdom
               <sup>13</sup>Instituto de Astrofisica de Canarias, E-38205 La Laguna, Tenerife, Spain
         <sup>14</sup>Universidad de La Laguna, Dpto. Astrofísica, E-38206 La Laguna, Tenerife, Spain
<sup>15</sup>Institut de Física d'Altes Energies (IFAE), The Barcelona Institute of Science and Technology, Campus
                                UAB, 08193 Bellaterra (Barcelona) Spain
              <sup>16</sup>Institut d'Estudis Espacials de Catalunya (IEEC), 08034 Barcelona, Spain
  <sup>17</sup>Department of Astronomy and Astrophysics, University of Chicago, Chicago, Illinois 60637, USA
     <sup>18</sup>NASA Goddard Space Flight Center, 8800 Greenbelt Rd, Greenbelt, Maryland 20771, USA
 <sup>19</sup>Jodrell Bank Center for Astrophysics, School of Physics and Astronomy, University of Manchester,
                          Oxford Road, Manchester, M13 9PL, United Kingdom
<sup>20</sup>University of Nottingham, School of Physics and Astronomy, Nottingham NG7 2RD, United Kingdom
<sup>21</sup>Astronomy Unit, Department of Physics, University of Trieste, via Tiepolo 11, I-34131 Trieste, Italy
        <sup>22</sup>INAF-Osservatorio Astronomico di Trieste, via G. B. Tiepolo 11, I-34143 Trieste, Italy
        <sup>23</sup>Institute for Fundamental Physics of the Universe, Via Beirut 2, 34014 Trieste, Italy
   <sup>24</sup>Hamburger Sternwarte, Universität Hamburg, Gojenbergsweg 112, 21029 Hamburg, Germany
   <sup>25</sup>School of Mathematics and Physics, University of Queensland, Brisbane, QLD 4072, Australia <sup>26</sup>Department of Physics, IIT Hyderabad, Kandi, Telangana 502285, India
        <sup>27</sup>Fermi National Accelerator Laboratory, P. O. Box 500, Batavia, Illinois 60510, USA
```

```
<sup>28</sup>Department of Physics and Astronomy, University of Waterloo,
                        200 University Ave W, Waterloo, ON N2L 3G1, Canada
         <sup>29</sup>Department of Physics, University of Michigan, Ann Arbor, Michigan 48109, USA
               California Institute of Technology, 1200 East California Blvd, MC 249-17,
                                    Pasadena, California 91125, USA
<sup>31</sup>Departments of Statistics and Data Sciences, University of Texas at Austin, Austin, Texas 78757, USA
<sup>32</sup>NSF-Simons AI Institute for Cosmic Origins, University of Texas at Austin, Austin, Texas 78757, USA
            <sup>33</sup>SLAC National Accelerator Laboratory, Menlo Park, California 94025, USA
  <sup>34</sup>Instituto de Fisica Teorica UAM/CSIC, Universidad Autonoma de Madrid, 28049 Madrid, Spain
                      <sup>35</sup>Universität Innsbruck, Institut für Astro- und Teilchenphysik,
                               Technikerstr. 25/8, 6020 Innsbruck, Austria
<sup>36</sup>Center for Astrophysical Surveys, National Center for Supercomputing Applications, 1205 West Clark
                                     St., Urbana, Illinois 61801, USA
               <sup>37</sup>Department of Astronomy, University of Ilinois at Urbana-Champaign,
                           1002 W. Green Street, Urbana, Illinois 61801, USA
         <sup>38</sup>School of Physics and Astronomy, Cardiff University, CF24 3AA, United Kingdom
              Santa Cruz Institute for Particle Physics, Santa Cruz, California 95064, USA
            <sup>40</sup>Center for Cosmology and Astro-Particle Physics, The Ohio State University,
                                       Columbus, Ohio 43210, USA
          <sup>41</sup>Department of Physics, The Ohio State University, Columbus, Ohio 43210, USA
                 <sup>2</sup>Department of Astronomy/Steward Observatory, University of Arizona,
                     933 North Cherry Avenue, Tucson, Arizona 85721-0065, USA
                    <sup>43</sup>Jet Propulsion Laboratory, California Institute of Technology,
                        4800 Oak Grove Dr., Pasadena, California 91109, USA
   <sup>44</sup>Centre for Gravitational Astrophysics, College of Science, The Australian National University,
                                        Acton ACT 2601, Australia
        <sup>45</sup>The Research School of Astronomy and Astrophysics, Australian National University,
                                        Acton ACT 2601, Australia
        <sup>46</sup>Departamento de Física Matemática, Instituto de Física, Universidade de São Paulo,
                              CP 66318, São Paulo, SP, 05314-970, Brazil
    <sup>47</sup>Faculty of Physics, Ludwig-Maximilians-Universität, Scheinerstr. 1, 81679 Munich, Germany
 <sup>48</sup>Max Planck Institute for Extraterrestrial Physics, Giessenbachstrasse, 85748 Garching, Germany
   <sup>49</sup>George P. and Cynthia Woods Mitchell Institute for Fundamental Physics and Astronomy, and
 Department of Physics and Astronomy, Texas A&M University, College Station, Texas 77843, USA Department of Astrophysical Sciences, Princeton University,
                             Peyton Hall, Princeton, New Jersey 08544, USA
<sup>51</sup>Kavli Institute for Particle Astrophysics and Cosmology, P. O. Box 2450, Stanford University, Stanford,
                                          California 94305, USA
                 <sup>52</sup>LPSC Grenoble—53, Avenue des Martyrs, 38026 Grenoble, France
            <sup>53</sup>Institució Catalana de Recerca i Estudis Avançats, E-08010 Barcelona, Spain
           <sup>54</sup>Department of Physics, University of Cincinnati, Cincinnati, Ohio 45221, USA
<sup>55</sup>Perimeter Institute for Theoretical Physics, 31 Caroline St. North, Waterloo, Ontario N2L 2Y5, Canada
      <sup>56</sup>Observatório Nacional, Rua Gal. José Cristino 77, Rio de Janeiro, RJ—20921-400, Brazil
     <sup>57</sup>Department of Physics, Carnegie Mellon University, Pittsburgh, Pennsylvania 15312, USA
          Ruhr University Bochum, Faculty of Physics and Astronomy, Astronomical Institute,
                 German Centre for Cosmological Lensing, 44780 Bochum, Germany
                <sup>59</sup>Nordita, KTH Royal Institute of Technology and Stockholm University,
                         Hannes Alfvéns väg 12, SE-10691 Stockholm, Sweden
             <sup>60</sup>Department of Physics, University of Arizona, Tucson, Arizona 85721, USA
          <sup>61</sup>Physics Department, Lancaster University, Lancaster, LA1 4YB, United Kingdom
           <sup>62</sup>Computer Science and Mathematics Division, Oak Ridge National Laboratory,
                                    Oak Ridge, Tennessee 37831, USA
           <sup>63</sup>Department of Physics, Duke University Durham, North Carolina 27708, USA
           <sup>64</sup>Department of Astronomy, Ohio State University, Columbus, Ohio 43210, USA
                     <sup>65</sup>Department of Astronomy, University of California, Berkeley,
                          501 Campbell Hall, Berkeley, California 94720, USA
   <sup>66</sup>Lawrence Berkeley National Laboratory, 1 Cyclotron Road, Berkeley, California 94720, USA
<sup>67</sup>Department of Physics, Stanford University, 382 Via Pueblo Mall, Stanford, California 94305, USA
       <sup>68</sup>Universitäts-Sternwarte, Fakultät für Physik, Ludwig-Maximilians Universität München,
                                Scheinerstr. 1, 81679 München, Germany
```

⁶⁹Department of Physics, Southern Methodist University, Dallas, Texas 75205, USA 70 Université Grenoble Alpes, CNRS, LPSC-IN2P3, 38000 Grenoble, France 71 Department of Astrophysical Sciences, Princeton University, Peyton Hall, Princeton, New Jersey 08544, USA

(Received 14 April 2025; accepted 2 June 2025; published 17 October 2025)

Galaxy clusters provide a unique probe of the late-time cosmic structure and serve as a powerful independent test of the ΛCDM model. This work presents the first set of cosmological constraints derived with ~16, 000 optically selected redMaPPer clusters across nearly 5000 deg² using DES year 3 datasets. Our analysis leverages a consistent modeling framework for galaxy cluster cosmology and DES-Y3 joint analyses of galaxy clustering and weak lensing (3 × 2pt), ensuring direct comparability with the DES-Y3 3×2 pt analysis. We obtain constraints of $S_8 = 0.864 \pm 0.035$ and $\Omega_{\rm m} = 0.265^{+0.019}_{-0.031}$ from the cluster-based data vector. We find that cluster constraints and $3 \times 2pt$ constraints are consistent under the ΛCDM model with a posterior predictive distribution (PPD) value of 0.53. The consistency between clusters and $3 \times 2pt$ provides a stringent test of ACDM across different mass and spatial scales. Jointly analyzing clusters with 3×2 pt further improves cosmological constraints, yielding $S_8 = 0.811^{+0.022}_{-0.020}$ and $\Omega_m = 0.294^{+0.022}_{-0.033}$, a 24% improvement in the $\Omega_m - S_8$ figure of merit over 3 × 2pt alone. Moreover, we find no significant deviation from the Planck CMB constraints with a probability to exceed (PTE) value of 0.6, significantly reducing previous S_8 tension claims. Finally, combining DES 3 \times 2pt, DES clusters, and Planck CMB places an upper limit on the sum of neutrino masses of $\sum m_{\nu} < 0.26$ eV at 95% confidence under the Λ CDM model. These results establish optically selected clusters as a key cosmological probe and pave the way for cluster-based analyses in upcoming stage-IV surveys such as LSST, Euclid, and Roman.

DOI: 10.1103/3dzh-d8f5

I. INTRODUCTION

The standard Λ CDM model of cosmology has been successful in explaining a wide range of observational results [1–14] (see [15–19] for reviews). However, recent evidence has started to hint the limitation of ACDM. Specifically, tension has emerged in the measurements of the S_8 parameter, the amplitude of the matter density fluctuations, defined as $S_8 = \sigma_8 \sqrt{\Omega_{\rm m}/0.3}$. The measurements of S_8 derived from the cosmic microwave background (CMB) [8], when converted to today's values, tend to be higher than the late-universe values directly measured from large-scale structure [20–27]; see [28–30] for reviews. Possible explanations of the tension range from unexpectedly strong baryonic feedback to beyond ACDM physics [31–33]. Another hint arises from measurements of the Hubble constant using local distance ladders, which yield a higher value than the one inferred from the CMB [e.g., [34]]. Moreover, recent combinations of Type-Ia supernovae (SN), baryonic acoustic oscillations (BAO), and CMB show hints that the dark energy, which drives the Universe's accelerated expansion, might not be a cosmological constant (Λ) [35,36].

To confirm or resolve the tension and to seek new physics beyond ΛCDM, we must examine the Universe from multiple perspectives. Galaxy clusters (CL), galaxy clustering (GC), and weak gravitational lensing (WL)

*Contact author: des-publication-queries@fnal.gov

are each sensitive to different aspects of the late-time cosmic structure. Consistently analyzing, comparing, and combining insights from all these probes forms the foundation of multiprobe cosmological analysis and is a key goal of the Dark Energy Survey [10,36–38]. Among these probes, galaxy clusters are megaparsec scale structures that probe the late-time cosmic structure and have long been recognized as a powerful cosmological probe [16,39–42]. Cosmological analyses have been conducted using clusters identified in x-ray [43–47], millimeter [48–50], and optical surveys [51–56].

Wide-field imaging surveys, such as the Dark Energy Survey (DES), the Hyper Suprime Cam (HSC), and the Kilo-Degree Survey (KiDS), simultaneously provide a large sample of optically identified clusters and the gravitational lensing signal for cluster mass calibration. Forecasts have shown that the clusters have a statistical power comparable to that of combined CMB + SN + BAO + WL in stage-III and stage-IV experiments [16]. However, despite its superb statistical power, optical cluster samples face unique challenges in systematic uncertainties. Previous analyses have revealed that clusters selected by optical richness tend to suffer a selection bias in lensing [57]. Specifically, without taking the selection bias in lensing into account, the cosmological constraints of σ_8 and $\Omega_{\rm m}$ in the DES-Y1 small-scale analysis [57] can be biased by more than 2σ . Recent analyses have treated the cluster selection bias using either analytic or simulationbased approaches [55,58,59].

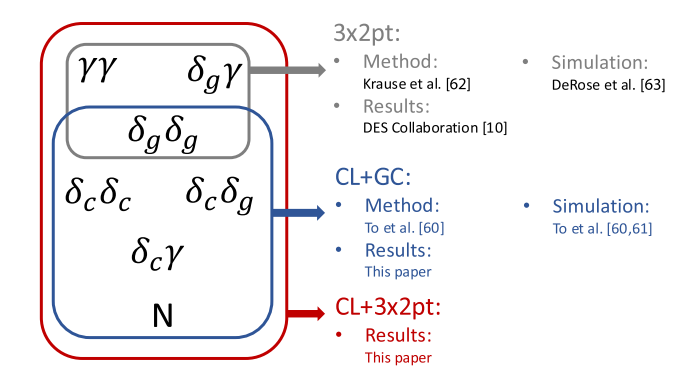


FIG. 1. Summary of the different components in this analysis. The data in this paper consist of cluster abundances (N) and six two-point correlation functions derived from galaxy density (δ_g), weak gravitational lensing shear (γ), and cluster density (δ_c). The correlation functions include cosmic shear ($\gamma\gamma$), galaxy-galaxy lensing ($\delta_g\gamma$), galaxy clustering ($\delta_g\delta_g$), cluster-galaxy cross-correlation ($\delta_c\delta_g$), cluster autocorrelation ($\delta_c\delta_c$), and cluster lensing ($\delta_c\gamma$). To facilitate the reader, we add references to supporting papers in the figure [10,60–63].

In this paper, we present the cosmological constraints from galaxy clusters using the first three years of observations from the Dark Energy Survey (DES-Y3). Specifically, we jointly analyze the cluster-based data vector (CL + GC¹ hereafter), including cluster abundances, large-scale cluster lensing, large-scale cluster-clustering, large-scale cluster-galaxy correlation functions, and large-scale galaxy-galaxy correlations, measured for DES-Y3 dataset (see Fig. 1 for a summary). As demonstrated in DES-Y1 [11], this combination of data vectors enables efficient and robust extraction of cosmological information from galaxy clusters. Specifically, cluster-galaxy crosscorrelations, cluster clustering, and galaxy clustering constrain cluster masses through the halo bias-halo mass relation, while cluster lensing provides an independent mass constraint. Together, these observables self-calibrate selection effects and yield precise cluster mass estimates. The resulting constraints on cluster mass and abundance lead to competitive cosmological constraints.

The DES-Y3 cluster sample consists of ~16 K redMaPPer² clusters across nearly 5000 deg², nearly tripling the sample size of DES-Y1. This increased statistical power necessitates the advancements in our modeling framework beyond DES-Y1 [11,58]. Our updated analysis, validated for the precision expected in the full DES dataset [60], addresses selection biases through a combination of optimized scale cuts and an improved analytic model. This approach is further validated through

analytic calculations and simulations [61]. Additionally, we employ a specially designed machine learning-based likelihood inference tool [64], reducing computational costs by a factor of 10. Parallel to this paper, the DES Galaxy Cluster team is working on extracting cosmology from small-scale cluster lensing while addressing systematics impacting small-scale lensing [59,65–73].

Leveraging this new cluster-based constraint alongside galaxy clustering and weak gravitational lensing measured from DES-Y3, we perform a stringent test of the ΛCDM model. Uniquely, our cluster cosmology analysis employed a fully consistent model with DES-Y3 $3 \times 2pt$, and we have homogenized analysis choices between clusters and 3 × 2pt. This enables relatively straightforward comparisons between cluster constraints and those from $3 \times 2pt$, as well as the joint analyses. Similar to DES-Y1, our joint analyses fully account for cross-covariance between different cosmological probes. The full data vector $(CL + 3 \times 2pt^4 \text{ hereafter})$ includes all data in CL + GC, high redshift galaxy clustering, galaxy-galaxy lensing, and cosmic shear (see Fig. 1 for a summary). We find that adding clusters leads to 24% improvements in cosmological constraints in the $\Omega_{\rm m}$ - S_8 plane.

This paper is organized as follows. We first present the dataset in Sec. II and then the measurement and modeling in Sec. III. We discuss our blinding strategies in Sec. IV. The cosmological results are presented in Sec. V. We conclude in Sec. VI. Appendix A presents a DES-Y3 catalog update. Appendix B shows the full sets of data vectors. Appendix C details the calculation of the posterior predictive distribution, which has been used to quantify the goodness of fit and the tension between correlated datasets. Appendix D discusses the constraints on the mass-richness relation. The constraints on nuisance parameters are presented in Appendix E.

II. DARK ENERGY SURVEY DATA

In this paper, we use a number of data products from the Dark Energy Survey year 3 (DES-Y3) dataset, which comprises data taken in the first three years of DES between 2013 to 2016. The foundation of the data products described here is the DES-Y3 Gold catalog described in [74], from which we derive the three samples of objects: the redMaPPer galaxy cluster sample (Sec. II A), the Metacalibration source galaxy sample, and the Maglim lens galaxy sample (Sec. II B). We note that the source and the lens galaxy samples have been described in detail in previous work [see [10] and references therein], so we therefore only summarize briefly the key aspects of the samples.

 $^{^{1}}$ We note that this was referred to as $4 \times 2pt + N$ in DES-Y1 [11].

²redMaPPer stands for the red-sequence matched-filter probabilistic percolation cluster finding algorithm.

 $^{^{3}}$ The 3×2 pt refers to the joint analyses of cosmic shear, galaxy clustering, galaxy-galaxy lensing.

⁴We note that this was referred to as $6 \times 2pt + N$ in DES-Y1 [11].

A. DES cluster samples

For this analysis, we use a volume-limited sample of galaxy clusters detected in DES-Y3 photometric data [75] with the redMaPPer cluster finder (v6.4.22 + 2). The redMaPPer algorithm operates on a subset of high-quality objects selected from the DES-Y3 Gold catalog. To ensure data quality, we exclude objects flagged with FLAG_GOLD = 8, 16, 32, or 64. We further select extended objects using the criterion EXTENDED_CLASS_MASH_SOF ≥ 2 . For photometry, we adopt the "single-object fitting" (SOF) measurements in the q, r, i, and z bands to identify clusters. Notably, this approach differs from DES-Y1 analyses, which relied on the multiepoch, multiobject fitting (MOF) composite model (CM) galaxy photometry. We opt for SOF photometry in this study because it demonstrates greater stability for bright central galaxies.

redMaPPer identifies galaxy clusters as overdensities of red-sequence galaxies. The cluster-finding process involves two main steps. First, the algorithm constructs an empirical red-sequence model, which relates galaxy colors to redshift. This model is derived using spectroscopic redshifts from the 14th data release of the Sloan Digital Sky Survey (SDSS DR14) [76] and the Australian Dark Energy Survey Global Redshift Catalog (OzDES GRC). Second, the algorithm iteratively identifies overdensities of red-sequence galaxies through a matched-filter technique. The matched filter consists of galaxy colors, positions, and luminosities, which are calculated from the SOF photometry and the red-sequence model.

Each detected galaxy overdensity, known as the redMaPPer cluster, is then assigned a photometric redshift (z_{λ}) , a mass proxy (richness, λ), and a central position based on the matched-filter likelihood. These properties form the basis for our subsequent cluster analyses.

In this analysis, we only use galaxy clusters with $\lambda > 20$ to ensure > 99% purity of the sample [77,78]. We further restrict the samples to redshift intervals $z_{\lambda} = [0.2, 0.65]$. The redshift lower limit mitigates the degradation of redMaPPer performances due to the lack of *u*-band data, and the redshift upper limit ensures a relatively constant footprint across redshift and consistency of redMaPPer redshift bins and the galaxy samples used for cross-correlations. With these restrictions, a total of 18,005 galaxy clusters are included in the DES-Y3 redMaPPer cosmology catalog. Among 18,005 clusters, 1514 of those are removed after applying a joint mask used by the 3×2 pt analyses. This is 2.5 times as many clusters compared to the cosmological sample in DES-Y1 [57].

The redMaPPer v6.4.22+2 algorithm used in this analysis is similar to the one used in DES-Y1 analyses [57,79] with one important update. The percolation radius,

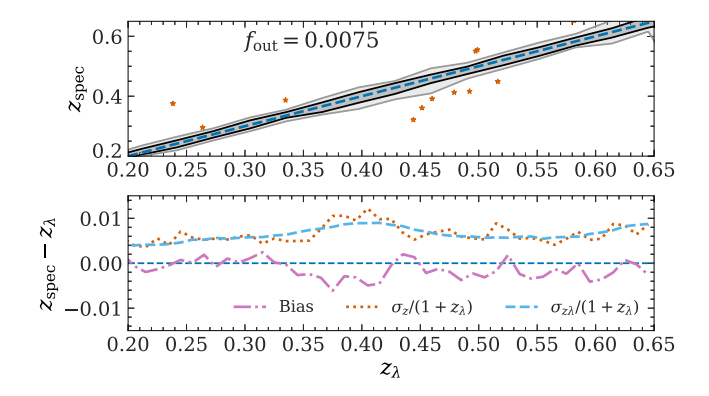


FIG. 2. Photometric redshift performance of DES-Y3 red-MaPPer cluster catalog. Upper panel: gray contours show 1σ and 2σ confidence intervals, and orange stars show 5σ outliers. Bottom: photo-z bias and uncertainties evaluated with available 1955 spectroscopic central galaxies. The orange line is estimated via the standard deviation of spectroscopic redshifts. The blue line is evaluated based on the reported redshift uncertainties estimated by redMaPPer.

the radius used to deblend overlapping redMaPPer clusters, is updated from $1.5 \times (\lambda/100)^{0.2} h^{-1}$ Mpc to $1.95 \times (\lambda/100)^{0.45} h^{-1}$ Mpc to be more consistent with the halo exclusion criteria in [80].

We further investigate the performance of DES-Y3 redMaPPer using available spectroscopic samples and DES-Y1 redMaPPer cluster samples. Figure 2 shows the redshift performance of the redMaPPer samples. We compare z_{λ} with the available central galaxies' spectroscopic redshift to estimate the redshift biases and scatters. In total, 1955 of DES-Y3 redMaPPer clusters have a spectroscopic central galaxy, and 194 of them have redshifts greater than 0.6. Using these samples, we find nearly unbiased redshifts with tight scatter $\sigma(z_{\lambda})/(1+z_{\lambda}) \simeq$ 0.006, consistent with [79]. Next, we compare in Fig. 3 the richness and redshifts of redMaPPer samples in DES-Y3 and DES-Y1 that have central galaxies within 0.5 arcmin separation. In this comparison, we use the DES-Y1 redMaPPer with $\lambda \geq 5$ to avoid loss of clusters from the sample due to scattering across the $\lambda = 20$ cut in DES-Y3 redMaPPer samples. We find that the two samples have consistent redshift but slightly different richness distributions. While the median values of the redshift ratio and richness ratio between DES-Y3 and DES-Y1 are similarly consistent with 1, we find that the scatter of the richness ratio is much more asymmetric and skewed toward larger values. This is likely due to differences in photometries and percolation radius used in the redMaPPer algorithm.

We note that the performance of DES-Y3 redMaPPer has been investigated in several companion papers. The centering efficiency is studied using XMM-Newton and

⁵The catalog is released at https://des.ncsa.illinois.edu/releases/y3a2/Y3key-cluster.

⁶We find a consistent result with 0.1 arcmin.

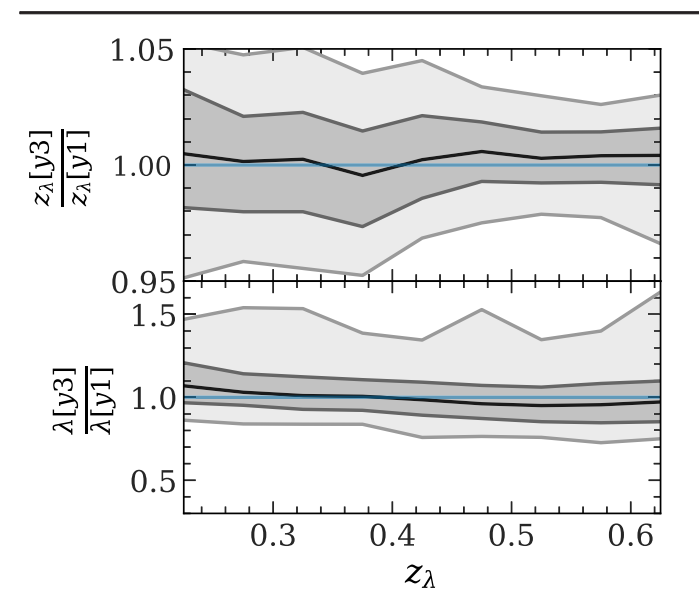


FIG. 3. Comparison of DES-Y1 redMaPPer and DES-Y3 redMaPPer samples that have central galaxy with < 0.5 arcmin seperation. Top panel: ratio of redshifts. Bottom panel: ratio of richness. Contours show 1σ and 2σ scatters. Black solid lines show the median.

Chandra x-ray imaging in [71]. The fraction of correctly centered redMaPPer clusters is 0.87 ± 0.04 . The distribution of radial offsets of miscentered clusters is modeled as a gamma distribution with a characteristic length scales of $0.23 \pm 0.05 R_{\lambda}$, where R_{λ} is the cluster radius estimated by redMaPPer. References [71,81] investigate the x-ray temperature-richness scaling relations, finding a tight relation with a scatter of 0.23 ± 0.01 and 0.21 ± 0.01 , respectively. Further, in [82], the authors quantify the performance of the redMaPPer cluster finder by crossmatching DES-Y3 clusters with detections from three South Pole Telescope surveys (SZ, pol-ECS, pol-500d). Specifically, they confirm a ~20%-40% bias on the richness estimate due to systems in projection [57] and rule out significant contamination by unvirialized objects at the high-richness end ($\lambda > 100$).

Finally, we quantify the selection function using a customized random catalog following the method in [83]. This random catalog is essential when constructing cluster-related two-point correlations. A key challenge in constructing cluster randoms is that clusters are extended objects whose detectability depends on their size, redshift, and survey boundaries. To address this, we generate redMapper randoms by sampling cluster richness-redshift pairs from the data and placing them at random positions. In this process, we ensure that each cluster is assigned a location where it could have been detected based on the survey redshift mask, a footprint-dependent redshift

upper limit below which all cluster member galaxies are above the detection limit. We then apply the same selection cuts as the redMaPPer cosmology sample, removing clusters whose masked fraction exceeds 0.2 or whose richness falls below 20. To correct the impact of these cuts on the redshift and richness distributions, we reweight each remaining cluster with the following procedure. Each cluster richness-redshift pair is repeatedly positioned at different places within the survey footprint 1000 times. We calculate the fraction of the 1000 repeated samples that pass the selection criteria mentioned above. This fraction is then used as the weight for that simulated cluster. This procedure ensures that the final random catalog has a consistent selection function as the cluster cosmology sample while properly accounting for survey boundaries and depth variations.

B. DES source and lens galaxy samples

We use the same source and lens galaxy samples as those used in [10] (see Appendix A for a minor update to the source catalog). Using the same sample is the key to cleanly and coherently combining the cluster information with the $3 \times 2pt$ information.

The Metacalibration source sample is derived from the Metacalibration algorithm [84] and rigorously examined in [85]. The final catalog consists of ~100 M galaxies divided into four tomographic bins. The weighted source number density is $n_{\rm eff} = 5.59$ gal/arcmin², with a corresponding shape noise of $\sigma_e = 0.261$. The redshift distribution and its calibration using independent methods based on photometry as well as clustering information is described in [86,87]. Using image simulations, [88] quantified the uncertainty in the shear calibration as well as its coupling with the redshift distribution due to blending.

The Maglim lens sample is constructed via a redshiftdependent magnitude selection from the DES-Y3 Gold catalog and is designed to have the maximum statistical power while maintaining control over the redshift uncertainties [89]. To minimize spurious clustering coming from spatially varying systematic effects, [90] derives a largescale structure weight that is included with the catalog. The definition of the bins as well as the redshift distribution and its uncertainty are derived using the directional neighborhood fitting (DNF) algorithm [91]. The original sample includes six tomographic bins. In [10], only four out of six redshift bins were used in the final cosmology analysis due to poor fits in the high-redshift bins. In this work, we further exclude the highest-redshift bin (bin 4) when crosscorrelating with the cluster sample due to the lack of overlap in redshift.

Table I lists the key characteristics of the source and lens sample, while Fig. 4 shows the redshift distribution of the samples. Constraints on the shear and redshift calibration parameters are listed in Table II.

⁷We specifically test the impact of this bias in richness on cosmological constraints in [60].

TABLE I. Basic characteristics of the source galaxy samples, lens galaxy samples, and cluster samples. The cluster sample has three tomographic bins, while each galaxy sample has four tomographic bins. For the lenses, we list the redshift range, total galaxy number counts, and number density. For the sources, we list the total number of galaxy counts, as well as the effective number density and shape noise for weak lensing. The area of the survey is 4, 143 deg².

redMaPPer clusters		
Bin	Redshift range	$N_{ m cluster}$
1	[0.2, 0.4]	5,632
2	[0.4, 0.55]	6,308
3	[0.55, 0.65]	4,551

Mag11m galaxies			
Bin	Redshift range	$N_{ m gal}$	$n_{\rm gal} ({\rm arcmin}^{-2})$
1	[0.2, 0.4]	2,236,473	0.1499
2	[0.4, 0.55]	1,599,500	0.1072
3	[0.55, 0.7]	1,627,413	0.1091
4	[0.7, 0.85]	2,175,184	0.1458

Metacalibration source galaxies			
Bin	$N_{ m gal}$	$n_{\rm eff}$ (arcmin ⁻²)	σ_{ϵ}
1	24,940,465	1.476	0.243
2	25,280,405	1.479	0.262
3	24,891,859	1.484	0.259
4	25,091,297	1.461	0.301

III. DATA VECTORS AND MODELING STRATEGY

A. Measurements

We split the sample of 16,491 DES-Y3 clusters within the DES-Y3 3 × 2pt footprint into three redshift bins in the range 0.2 < z < 0.65. Within each tomographic bin, the clusters are further split into four richness bins, $20 \le \lambda < 30, 30 \le \lambda < 45, 45 \le \lambda < 60, 60 \le \lambda$. The corresponding number counts N are shown in Appendix B; these 12 data points have a combined signal to noise (SNR) of 94.5. For all summary statistic measurements, presented in the figures shown in Appendix B, each panel shows the data points in the upper part and the fractional difference between the data and the mean of the predictions from the CL + GC chains, normalized by the PPD prediction scatter (Appendix C). Data points excluded from the analysis by scale cuts are shown in light opacity.

We use the TreeCorr code [92] to measure two-point autoand cross-correlation functions of the DES-Y3 cluster sample, the Maglimlens sample, and the Metacalibration source sample. As mentioned in Sec. IIB, the CL+GCanalysis restricts the lens galaxy sample to Maglim tomography bins 1–3, as Maglim bin 4 does not overlap with the cluster redshift range 0.2 < z < 0.65, and

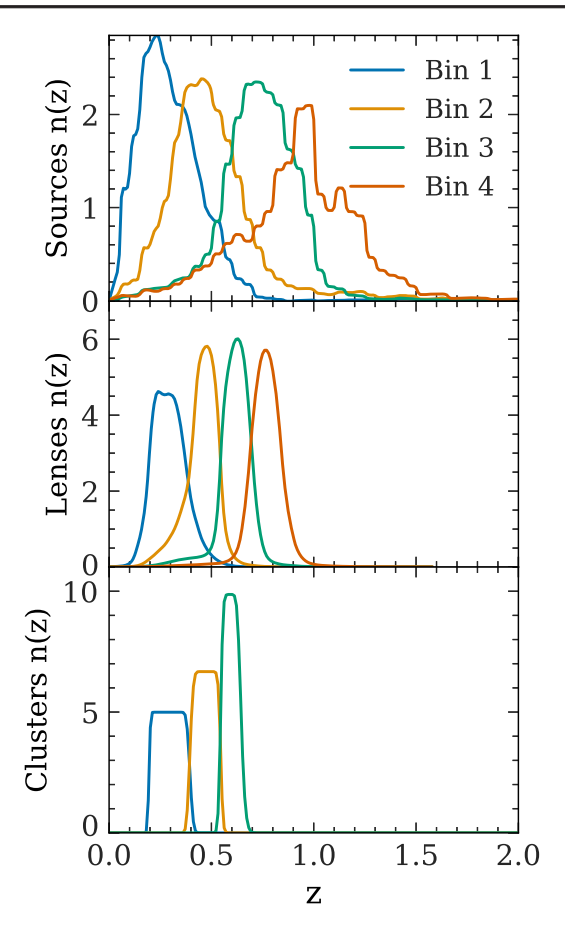


FIG. 4. The Metacalibration source galaxy (top), Maglim lens galaxy (middle), and redMaPPer cluster (bottom) redshift distributions.

we do not detect a cross-correlation at the sensitivity in this analysis.

The resulting two-point statistics are $\gamma_c(\theta)$, the tangential shear profile per cluster richness bin and cluster-source tomography bin combination (with 404 data points after scale cuts and a SNR of 31.8), w_{cc} , the angular clustering of clusters across richness bins within each tomography bin (with 149 data points after scale cuts and a SNR of 18.8), and w_{cg} , the angular cross-clustering of clusters and galaxies per cluster richness bin and cluster-galaxy tomography bin combination (with 124 data points after scale cuts and a SNR of 39.6). We use measurements of the Maglim angular correlation function $w_{\rm gg}$ from [90] (31 data points after scale cuts and a SNR of 52.5), which we reproduce in the figure presented Appendix B to illustrate the fractional difference between $w_{\rm gg}$ and the mean of the predictions from the CL + GC chains. All two-point measurements are presented in Appendix B.

B. Modeling strategy

The theoretical model for the CL + GC and $CL + 3 \times 2pt$ analyses is described in detail and validated in [60], building

on the $3 \times 2pt$ model [62,93]. Briefly, the $3 \times 2pt$ model is based on a model for the nonlinear matter power spectrum, linear galaxy bias, the tidal alignment tidal torquing (TATT) intrinsic alignment model [94], which is an extension of the nonlinear alignment (NLA) model. The massive neutrinos are modeled as three degenerate species of equal mass. Our model further included magnification of lens galaxies, photometric redshift uncertainties parametrized by a shift parameter (Metacalibration) or shift and stretch parameters (Maglim), and multiplicative shear calibration uncertainty; nonlocal contributions to galaxygalaxy lensing from the mass distribution below the scale cut are marginalized out, which we implement as a parametric marginalization ("point mass"). The theoretical predictions for the cluster observables are calculated using a log-normal richness-mass relation and an empirical, scale-dependent model for redMaPPer selection effects (see Sec. C5 of [60] for details). The model for cluster 2pt-statistics (γ_c , w_{cc} , w_{cg}) is an extension of the $3 \times 2pt$ model, with the linear bias of each cluster richness bin computed from the observablemass relation and the halo bias-mass relation. The cluster lensing goes through a linear transformation based on the relation of the tangential shear profile ($\Delta\Sigma$) and the projected surface density (Σ) to localize the signal [95]. Scale cuts for cluster (cross-) clustering and cluster lensing are determined to control the impact of nonlinear biasing and uncertainties in the modeling of the nonlinear matter distribution.

The model parameters and priors are summarized in Table II. We note that compared to the DES-Y3 $3 \times 2pt$ analysis presented in [10], we implement two changes for consistency with the upcoming DES year 6 analyses: The matter power spectrum model is updated to HMCode2020 [96], and we employ weakly informative priors on the redshift evolution of intrinsic alignments (η_1, η_2) to reduce prior volume effects.

Simulated analyses of noise-less model vectors indicate that marginalized parameter constraints should only be weakly affected by prior volume effects, with the 2D marginalized constraint on $\Omega_{\rm m}$ and S_8 biased by less than 0.3 of the statistical uncertainties.

TABLE II. Parameters and priors considered in this analysis. "Flat" represents a flat prior in the given range, "Gauss (μ, σ) " denotes a Gaussian prior with mean μ and width σ , and "Fixed (X)" means that the parameter is fixed at X.

Parameter	Prior	Varied in CL + GC	Varied in $CL + 3 \times 2pt$
Cosmology			
$\Omega_{ m m}$	Flat (0.1, 0.9)	✓	✓
$A_s \times 10^9$	Flat (0.5, 5.0)	✓	✓
n_s	Flat (0.87, 1.07)	✓	✓
$\Omega_{ m b}$	Flat (0.03, 0.07)	✓	✓
h	Flat (0.55, 0.91)	✓	✓
$\Omega_{ u} h^2$	Flat (0.0006, 0.00644)	✓	✓
Galaxy bias			
$b_{1,1}^1$	Flat (0.8, 3.0)	✓	✓
$b_{1,1}^{2}$	Flat (0.8, 3.0)	✓	✓
$b_{1,1}^{3}$	Flat (0.8, 3.0)	✓	✓
$b_{1,1}^4$	Flat (0.8, 3.0)	•••	✓
Intrinsic alignme	ent		
a_1	Flat $(-5.0, 5.0)$	✓	✓
η_1	Gauss (0, 3)	✓	✓
a_2	Flat $(-5.0, 5.0)$	• • •	✓
η_2	Gauss (0, 3)	• • •	✓
b_{TA}	Fixed (1)	•••	• • •
Maglim photo-z			
$\Delta_{z,l}^1 \times 10^2$	Gauss $(-0.9, 0.7)$	✓	✓
$\Delta_{z,l}^{2} \times 10^2$	Gauss $(-3.5, 1.1)$	✓	✓
$\Lambda^3 \times 10^2$	Gauss $(-0.5, 0.6)$	✓	✓
$\Delta_{71}^{2,1} \times 10^2$	Gauss $(-0.7, 0.6)$	• • •	✓
$w_{z,1}^{\tilde{1}}$	Gauss (0.98, 0.06)	✓	✓
w_{71}^{2}	Gauss (1.31, 0.09)	✓	✓
w_{71}^{3}	Gauss (0.87, 0.05)	✓	✓
$\begin{array}{l} \Delta_{z,l} \times 10^{2} \\ \Delta_{z,l}^{4} \times 10^{2} \\ w_{z,l}^{1} \\ w_{z,l}^{2} \\ w_{z,l}^{3} \\ w_{z,l}^{4} \end{array}$	Gauss (0.92, 0.05)	•••	✓

(Table continued)

TABLE II. (Continued)

Parameter	Prior	Varied in CL + GC	Varied in $CL + 3 \times 2pt$
Maglim <i>magnifi</i>	ication		
C_1^1	Fixed (0.42)	•••	• • •
C_1^1 C_1^2 C_1^3 C_1^4	Fixed (0.30)	•••	•••
C_1^3	Fixed (1.76)	• • •	• • •
C_1^4	Fixed (1.94)	• • •	• • •
Point-mass marg	inalization		
B^i	Flat $(-1.0, 1.0)$	• • •	✓
Source galaxy ph	hoto-z		
$\Delta_{z,s}^1 \times 10^2$	Gauss (0.0, 1.8)	✓	✓
$\Delta_{z,s}^2 \times 10^2$	Gauss (0.0, 1.5)	✓	✓
$\Delta_{z,s}^3 \times 10^2$	Gauss (0.0, 1.1)	✓	✓
$\Delta_{z,s}^4 \times 10^2$	Gauss (0.0, 1.7)	✓	✓
Shear calibration	i		
$m_1 \times 10^2$	Gauss $(-0.6, 0.9)$	✓	✓
$m_2 \times 10^2$	Gauss $(-2.0, 0.8)$	\checkmark	✓
$m_3 \times 10^2$	Gauss $(-2.4, 0.8)$	✓	✓
$m_4 \times 10^2$	Gauss $(-3.7, 0.8)$	\checkmark	✓
redMaPPer rick	hness-mass relation		
$\ln \lambda_0$	Flat (2.0, 5.0)	✓	✓
$A_{\ln \lambda}$	Flat (0.1, 1.5)	\checkmark	✓
$B_{\ln \lambda}$	Flat $(-5.0, 5.0)$	√	✓
$\sigma_{ m intrinsic}$	Flat (0.1, 1.0)	✓	✓
redMaPPer sele			
b_{s1}	Flat (1.0, 2.0)	✓	✓
b_{s2}	Flat $(-1.0, 1.0)$	√	✓
r_0	Flat (10, 60)	✓	✓
redMaPPer ma			
$C^i_{\mathtt{c}_A}$	Fixed (-2)	•••	•••

The likelihood inferences are performed using a customized sampler LINNA [64]. LINNA automatically builds a theory emulator, iteratively modifies the training sample, and performs MCMC analyses. The accuracy of LINNA for 3×2 pt, CL + GC, and CL + 3×2 pt has been validated to the expected constraining power of LSST-Y10.

IV. BLINDING AND UNBLINDING

In this paper, the CL + GC portion of the analysis is done in a blinded fashion to avoid any implicit decisions based on the results from the data. The blinding and unblinding protocol was defined before making any measurements with data and followed to minimize any unintentional analysis decisions being affected by the data results. The philosophy follows what was done in [10,53]. Below, we describe the blinding strategies, the findings during unblinding, and any changes in the analysis after unblinding.

A. Blinding

As this analysis is done after the $3 \times 2pt$ analysis is unblinded [10], there is no catalog or data vector-level blinding. We only perform blinding at the parameter level.

That is, we run chains directly on the unblinded data vectors, but the output chain samples are shifted before being saved and analyzed.

For the cosmological parameters of interest ($\Omega_{\rm m}$, h, $\Omega_{\rm b}$, n_s , A_s , $\sum m_{\nu}$), we apply a random shift drawn from a uniform distribution with an upper limit of 5σ of the posterior of that parameter and a lower limit of 0. For the four mass-observable relation parameters ($\ln \lambda_0$, $A_{\ln \lambda}$, $B_{\ln \lambda}$, $\sigma_{\rm intrinsic}$) and the three galaxy bias parameters (only the first three lens bins were used in the CL + GC part), we apply the same procedure but with an upper limit of 2σ of the posterior.

Note that we do not blind all other parameters or the χ^2 values. We are allowed to plot the unblinded data vector and best-fit model without blinding, as well as the blinded contours.

B. Unblinding

To unblind, we have defined a list of tests that need to be passed. There are three main categories of tests that we describe below:

(1) *Modeling tests*: These tests check that we can recover unbiased cosmology with our modeling choices. In particular, they verify that with the scales

used in the analysis, we can recover unbiased cosmology even with uncertainty in some of the modeling choices. Most of these tests are carried out and thoroughly checked in [60] using simulated data vectors. In this paper, we conduct one additional test of the model.

(a) Redshift-dependent selection effect. We investigate whether the redshift evolution of the selection effect needs to be explicitly modeled. To do this, we introduce a redshift-dependent parameterization of the selection effect amplitude, b_{s1} [for the equation of the selection effect model, see Eq. (23) of [60]]:

$$b_{s1}\left(\frac{1+z}{1.45}\right)^{b_z},\tag{1}$$

where b_z is a free parameter governing the redshift evolution. If b_z is consistent with 0 within 3σ , we do not consider a redshift-dependent selection effect model. Repeating our CL + GC cosmological analysis with this modification, we obtain a marginalized 1σ constraint of $b_z = -0.04^{+0.29}_{-0.34}$, consistent with zero. The resulting cosmological constraints remain consistent with our fiducial analysis, as shown in the second row of Fig. 5. This result indicates that redshift evolution in the selection effects is negligible and has minimal impacts on cosmological constraints.

- (2) Data-level tests: These tests empirically examine whether there are any unexpected data behaviors. All the tests are thus run directly on the data itself. There are a number of tests here that we summarize. Overall, our results are summarized in Fig. 5, and we find that there are no significant issues in the data that prevent us from unblinding.
 - (a) Systematics weights. We test the effect of varying survey conditions, which might imprint an artificial clustering signal on the large-scale twopoint correlation functions. We expect this effect to be negligible for the CL + GC analysis due to the reasons below. First, cross-correlations such as cluster-galaxy cross-correlations and cluster lensing have much higher signal-to-noise than clustering of clusters. As long as the survey systematics on the galaxy sample are removed, the cross-correlations are immune from this systematics even if we do not correct the impact on the cluster density field. Second, the cluster randoms are constructed by injecting fake clusters on real data and rerunning the detection. This process is expected to remove most of the survey systematics for the relative density of clusters and randoms. To validate these expectations, we conduct an explicit test using DES-Y3 data. We first match redMaPPer, redMaPPer randoms, and broad- χ^2 redMaGiC samples [97] in DES-Y3 by their positions. The broad- γ^2 redMaGiC sample, one of the two lens galaxy samples in the DES-Y3 $3 \times 2pt$ cosmology

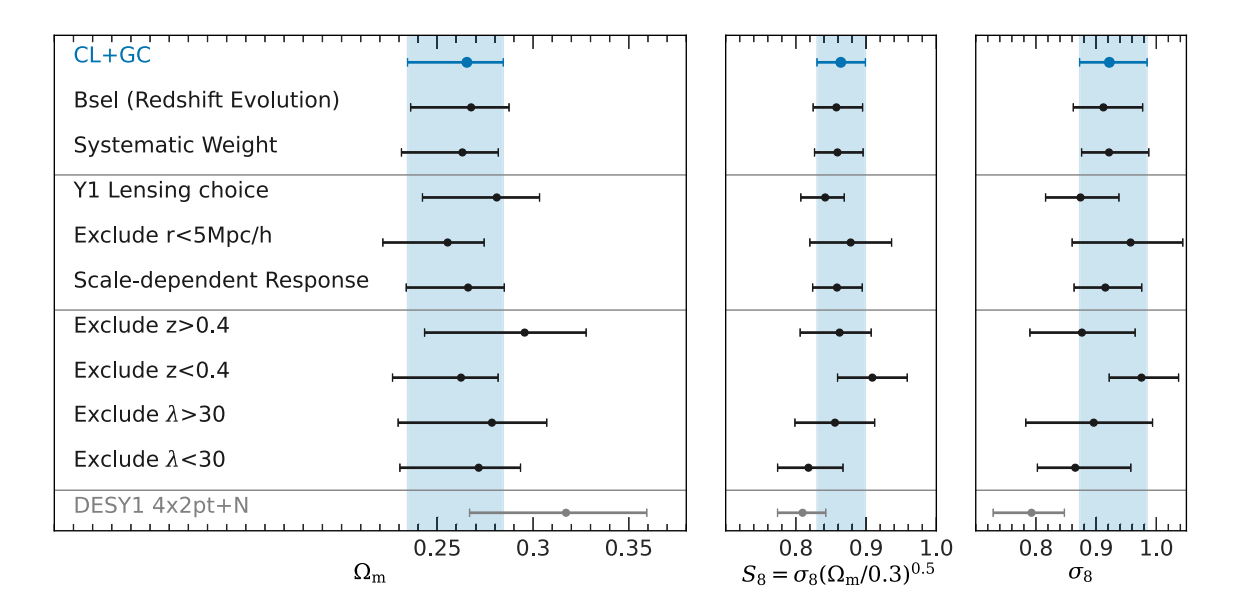


FIG. 5. Summary of marginalized constraints (mean and 1σ confidence interval) on S_8 , Ω_m , and σ_8 in Λ CDM. The first section shows additional modeling tests beyond those presented in [60]. The second section shows the impact of cluster lensing analysis choice, while the third section shows the consistency of different data splits. The final section shows the constraints from DES-Y1 data as a comparison.

- analyses, is selected for its color consistency with the redMaPPer red sequence model. We apply its systematic weights, which correct survey systematics in the redMaGiC galaxy density fields, to both the redMaPPer sample and its randoms. Using these weights, we generate a new data vector and compare the resulting cosmological constraints to those from our fiducial analysis. Because galaxies should be more affected by survey systematics than galaxy clusters, the difference between the two analyses sets an upper bound on the impact of systematics on the clustering signal for CL + GC. Since we expect negligible changes in cosmological constraints, our requirement for this test is that S_8 and $\Omega_{\rm m}$ constraints should shift within 0.3σ . We find that the difference in S_8 and $\Omega_{\rm m}$ constraints between the two analyses is 0.068σ , confirming that survey systematics have a negligible effect.
- (b) Cluster lensing estimator. Our analysis choices for cluster lensing are different from those of DES-Y1. We apply a linear transform [95] to localize the cluster lensing signal [60], and we adopt a scale cut $(2h^{-1} \text{ Mpc})$ on the transformed cluster lensing) that is different from Y1 $(8h^{-1} \text{ Mpc on } \gamma_c)$. We first test our analysis with DES-Y1 analysis choices [11,58], where we do not perform localized transform but adopt $8h^{-1}$ Mpc as our scale cut. We then assess whether including small-scale cluster lensing biases the cosmological constraints by repeating the analysis with the cluster lensing signal removed at $2-5h^{-1}$ Mpc. Since it is difficult to define the requirements for these tests, we qualitatively examine the posterior. If the shift in the $\Omega_{\rm m}$ -S₈ plane is greater than 3σ of the fiducial analysis, we investigate further.

As shown in Fig. 5, we find that Y1 analysis choices lead to higher Ω_{m} (mean $\Omega_{m}=0.27$ to 0.28) but lower σ_8 (mean $\sigma_8 = 0.92$ to 0.87). Reference [95] has shown that galaxy-galaxy lensing measurements contain one-halo contribution even at $12h^{-1}$ Mpc. Because structures near clusters are more nonlinear, we expect that cluster lensing contains even more one-halo contribution at $12h^{-1}$ Mpc. The Y1 analysis likely overestimates the lensing signal due to this residual one-halo contribution, leading to a bias toward higher Ω_m and correspondingly lower σ_8 to maintain the same cluster abundance. While adopting the DES-Y1 analysis choices does not fully shift the DES-Y3 cosmological constraints to match DES-Y1 results [11], the trend is consistent. The remaining difference is well within expectations from statistical

- fluctuations. Additionally, removing small-scale cluster lensing only mildly shifts the cosmological constraints, highlighting the robustness of our constraints to small-scale systematics once the cluster lensing signal is localized.
- (c) Scale-dependent Metacalibration sponse. We check whether using scale-dependent Metacalibration responses impacts our results. While the analyses of the South Pole Telescope (SPT) [49] and eROSITA [98] adopt a scale-dependent response, we choose to adopt a scale-independent response as our fiducial analysis choice. This is because it is unclear whether the measured scale-dependent response is due to the contribution of cluster member galaxies, which do not contribute to the lensing signal. Adopting a scale-dependent response could lead to a bias in cluster lensing measurement. Since it is unclear whether a scale-dependent response should be adopted, it is difficult to define the requirements for this test. Our threshold for unblinding is that the shift in the $\Omega_{\rm m}$ - S_8 plane between analyses with and without scaledependent responses is less than 3σ of the fiducial analysis. We show in Fig. 5 that this analysis choice leads to negligible impacts on our cosmological constraints.
- (d) Data split test. We perform the cosmological inference with a subset of the data to check for consistency. In particular, we split the cluster sample according to redshift (z < 0.4 and z > 0.4) and richness ($\lambda < 30$ and $\lambda > 30$). We also split the two-point data vector into subsets that contain lensing and clustering. Since it is difficult to define the requirements for this test, we qualitatively examine the posterior. Our threshold for unblinding is that the shift in the $\Omega_{\rm m}$ - S_8 plane between analyses of two subsets of the data is less than 3σ of the fiducial analysis. As shown in Fig. 5, all splits yield consistent cosmological constraints, reinforcing the robustness of our result.
- (e) Covariance matrix. We check that the implementation of the shape noise component in the covariance is consistent between an analytical calculation and that from randomly rotating the galaxies.
- (3) Goodness-of-fit tests: We want to test whether our model is a good description of the data. We have to predefine a course of action in the scenario that our model does not fit the data so that we do not make decisions in favor of the model we considered. In particular, we use the posterior predictive distribution (PPD) methodology described in Appendix C to evaluate the goodness of fit in a fully Bayesian way. We set the threshold for unblinding to be 0.01.

Once all the tests above were passed, we unblind the cosmological constraints for CL + GC. There have been no changes in the analysis after unblinding.

V. COSMOLOGICAL CONSTRAINTS

We employ DES cluster measurements and a thorough analysis pipeline presented in Sec. III to test the currently favored ΛCDM model (the five-parameter ΛCDM model with a varying neutrino mass). One unique aspect of DES-Y3 cluster constraints is that we homogenize analysis choices and systematic models between DES-Y3 clusters and DES-Y3 3 × 2pt cosmological analyses, enabling an apples-to-apples comparison between different cosmological probes and, eventually, joint analyses. In this section, we first discuss the robustness of DES cluster cosmology results and compare them with other optical, x-ray, and millimeter cluster cosmology constraints. We then discuss the consistency between DES clusters and other DES cosmological probes. Finally, we present results from joint analyses of clusters and $3 \times 2pt$ and compare them with cosmology from external datasets. Throughout this section, we use the PPD methodology to assess goodness-of-fit and evaluate consistency between different data vectors within a fully Bayesian framework (see Appendix C for details). A low PPD value (e.g., 0.01⁸) signals potential inconsistencies between the model and data or among different datasets.

A. DES-Y3 CL +GC cluster cosmology

In Fig. 6, we show the marginalized CL+GC constraints from the DES-Y3 redMaPPer clusters for σ_8 , S_8 , and $\Omega_{\rm m}$. The numerical values of the constraints are shown in Table III. We find that $\Lambda {\rm CDM}$ well describes DES-Y3 cluster measurements. Using the PPD metric [99] to quantify the goodness of fit (see Appendix C), we find $p(CL+GC|\Lambda {\rm CDM})=0.39$. Marginalized over 28 astrophysical parameters, CL+GC constraints on the key parameters are

$$\begin{split} S_8 &= 0.864 \pm 0.035 \\ \Omega_{\rm m} &= 0.265^{+0.019}_{-0.031} \\ \sigma_8 &= 0.922^{+0.063}_{-0.049}. \end{split} \tag{2}$$

The figure of merit⁹ on $\Omega_{\rm m}$ – S_8 of DES-Y3 CL + GC to DES-Y1 CL + GC is 1.52, which is expected by the improved statistical power [11].

We now compare our results with other optical cluster cosmology analyses in Fig. 6. Reference [55] calibrates redMaPPer clusters detected in SDSS using HSC-Y3

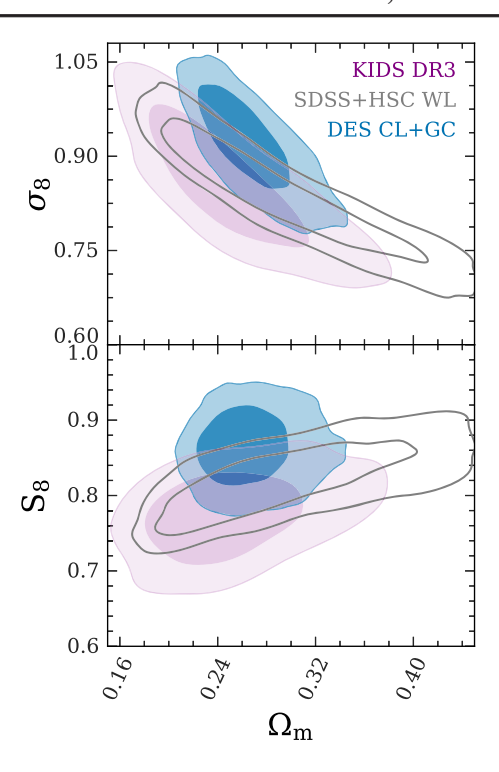


FIG. 6. Marginalized constraints on the three parameters σ_8 , $S_8 = \sigma_8 \sqrt{\Omega_{\rm m}/0.3}$, and $\Omega_{\rm m}$ in the $\Lambda{\rm CDM}$ model from stage-III optical cluster cosmology analyses. Contours show 68% and 95% confidence intervals.

weak lensing data, obtaining constraints that are broader but consistent with our CL + GC results. Similarly, Ref. [54] analyzes optically selected clusters in the KiDS survey using KiDS-DR3 weak lensing. While their constraints are also broader and consistent with DES CL + GC, they find a slightly lower value of S_8 . While we focus on comparisons with the latest results from optical clusters, we show comparisons of various DES cluster cosmology analyses in Appendix F.

Figure 7 extends this comparison to cluster cosmology constraints from different wavelengths. Reference [49] analyzes clusters detected in the SPT-SZ and SPTpol surveys, with mass calibration performed using DES-Y3 and HST weak lensing. Reference [47] studies clusters from the western Galactic hemisphere of eROSITA's first All-Sky Survey (eRASS1), calibrating masses with DES-Y3, KiDS, and HSC weak lensing datasets [98,100]. The figure of merit on $\Omega_{\rm m}$ -S₈ of DES-Y3 CL + GC to SPT and eRASS is 0.75 and 0.2, respectively. We find that our constraints are consistent with eRASS1 and SPT. The central value of S₈ from DES-Y3 clusters is similar to that of eRASS1 and is somewhat higher than SPT. Interestingly, the mean mass of DES-Y3 clusters is more similar to that of eRASS1 than SPT (see Fig. 18), and the redshift range of eRASS1 (z = 0.1-0.8) and DES-Y3 (z = 0.2-0.65) is more similar than SPT (z = 0.25-1.78). The consistent deviation of DES-Y3 and eRASS1 from SPT could suggest a massdependent or redshift-dependent trend in S_8 constraints

⁸Note that this is the unblinding criteria of the DES-Y3 $3 \times 2pt$ analysis [10].

The figure of metrit is calculated as $1/\sqrt{\det(\text{Cov}(S_8, \Omega_{\text{m}}))}$.

dots.				
Parameter	$3 \times 2pt$	CL + GC	$CL + 3 \times 2pt$	$CL + 3 \times 2pt + Planck CMB$
$\overline{\Omega_{ m m}}$	$0.332^{+0.032}_{-0.042}$	$0.265^{+0.019}_{-0.031}$	$0.294^{+0.022}_{-0.033}$	$0.317^{+0.007}_{-0.011}$
$A_s(\times 10^{-9})$	$1.988^{+0.232}_{-0.442}$	$2.527^{+0.323}_{-0.544}$	$2.068^{+0.249}_{-0.450}$	$2.092^{+0.028}_{-0.033}$
$\sum m_{\nu}$ (eV)	• • •	• • •	• • •	< 0.258(95%CL)
h			• • •	$0.672^{+0.008}_{-0.006}$
σ_8	$0.748^{+0.053}_{-0.063}$	$0.922^{+0.063}_{-0.049}$	0.822 ± 0.053	$0.790^{+0.016}_{-0.010}$
S_8	0.784 ± 0.022	0.864 ± 0.035	$0.811^{+0.022}_{-0.020}$	$0.812^{+0.012}_{-0.011}$

TABLE III. Summary of the marginalized parameter constraints in Λ CDM. The mean and 68% confidence interval are provided for each cosmological parameter. Parameters that are not constrained are indicated by a center dots.

derived from galaxy clusters. However, given the current statistical precision of DES-Y3, this remains an intriguing possibility rather than a definitive conclusion.

The DES-Y3 cluster cosmology analysis differs in key ways from most other cluster studies. For example, KiDS, HSC, eRASS, and SPT all rely on cluster lensing at scales below $2h^{-1}$ Mpc for mass calibrations, while DES-Y3 clusters remove those scales for analyses. DES-Y3 clusters uniquely incorporate cluster-galaxy cross-correlations for mass calibrations. DES-Y3 clusters consider the full modeling complexities of DES weak lensing analysis, while others simplify some of the modeling choices, such as intrinsic alignment, magnifications, etc., although we note

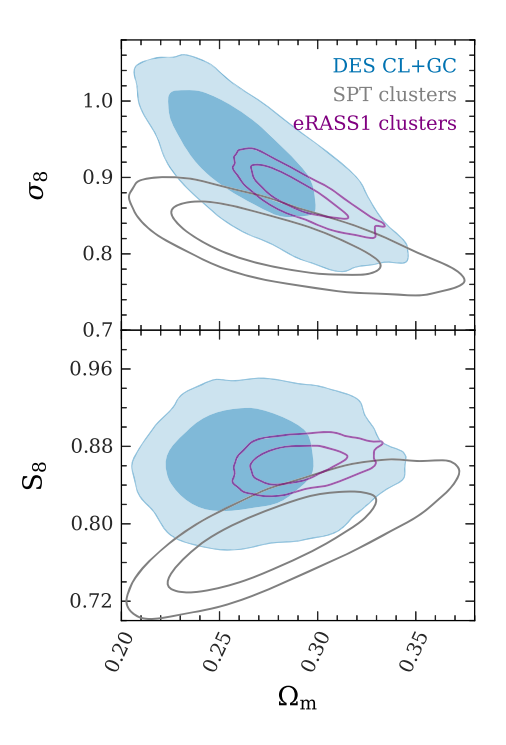


FIG. 7. Marginalized constraints on the three key parameters $\sigma_8,\,S_8=\sigma_8\sqrt{\Omega_m/0.3},\, \text{and}\,\,\Omega_m$ in the ΛCDM model from cluster cosmology analyses, including DES-Y3 clusters (blue), SPT-SZ+SPTpol clusters with DES-Y3 weak lensing mass calibrations (gray), and eRASS1 clusters with DES-Y3, HSC, and KiDS weak lensing mass calibrations (purple). Contours show 68% and 95% confidence intervals.

that our analysis approach is slightly more sensitive to these effects. Despite these differences, the level of consistency between DES-Y3 cluster cosmology and results from independent optical, x-ray, and SZ-selected cluster analyses is remarkable. This agreement, across diverse datasets and modeling assumptions, highlights the reliability and the great potential of galaxy clusters as a cosmological probe.

B. Consistency between CL + GC cluster cosmology constraints and 3 × 2pt in DES-Y3

We now turn to check the internal consistency between different DES cosmological probes. Using the PPD metric, we find $p(\xi_{\pm}|\text{CL}+\text{GC})=0.04$ and $p(\xi_{\pm}+\gamma_t[\text{first three bin}]|\text{CL}+\text{GC})=0.07$. We note that we cannot calculate the PPD of full 3×2 pt and CL+GC because of shared galaxy clustering data vectors and the lack of the bias value of the highest redshift bin of Maglim in CL+GC analyses. Finally, we check that the ΛCDM model fits to the combined data vector, obtaining $P(\text{CL}+\text{GC}|\Lambda\text{CDM})=0.53$. With all these tests, we established that DES-Y3 clusters and DES-Y3 3×2 pt are consistent under the ΛCDM model. This consistency itself is a remarkable cosmological test of the ΛCDM model because of the widely different masses and scales probed by different observables.

C. Cosmology from joint analyses of cluster abundances, weak lensing, and galaxy clustering

Having checked the consistency, we jointly analyze cluster abundances and all possible two-point correlation functions between cluster density, galaxy density, and weak lensing shear field, known as the $CL+3\times 2pt$ probes. The marginalized constraints on Ω_m , S_8 , and σ_8 are shown in Fig. 8 and summarized in Table III. Marginalized over 37 astrophysical parameters, the DES $CL+3\times 2pt$ constraints on the key parameters are

$$S_8 = 0.811^{+0.022}_{-0.020}$$

 $\Omega_{\rm m} = 0.294^{+0.022}_{-0.033}$
 $\sigma_8 == 0.822 \pm 0.053.$ (3)

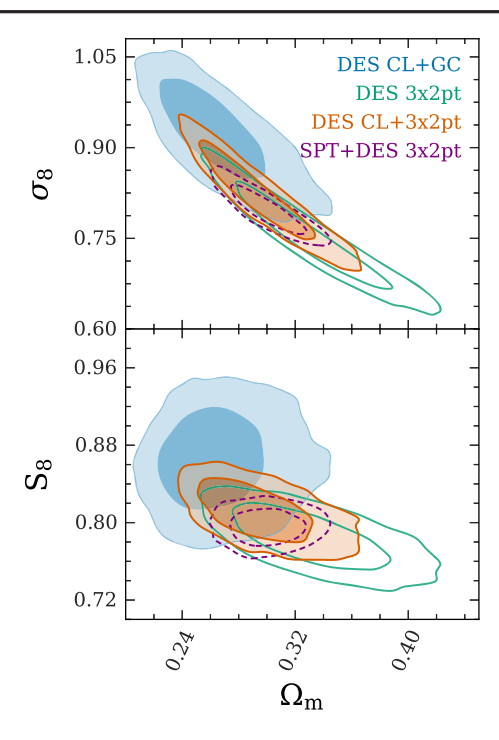


FIG. 8. Marginalized constraints on the three key parameters σ_8 , $S_8 = \sigma_8 \sqrt{\Omega_{\rm m}/0.3}$, and $\Omega_{\rm m}$ in the $\Lambda{\rm CDM}$ model from different DES cosmological probes, including DES-Y3 clusters (blue), DES-Y3 3 × 2pt (green), and joint analyses of DES-Y3 clusters and DES-Y3 3 × 2pt (orange). We further show combined analyses of SPT clusters and DES-Y3 3 × 2pt (purple). Contours show 68% and 95% confidence intervals.

The ratio of the figure of merit on $\Omega_{\rm m}$ – S_8 of DES-Y3 CL + 3×2 pt to DES-Y3 3×2 pt is 1.24. In addition to the improved constraining power, CL + 3×2 pt favors a higher S_8 and smaller $\Omega_{\rm m}$ value than that of 3×2 pt. In Fig. 8, we also compare our CL + 3×2 pt constraints with the combined analysis of SPT and DES-Y3 3×2 pt and find consistent results. The slightly better constraints of SPT and DES-Y3 3×2 pt are mostly due to a more orthogonal degeneracy direction between SPT and DES-Y3 3×2 pt than CL + GC and DES-Y3 3×2 pt.

Comparing the $CL + 3 \times 2pt$ with the prediction of ΛCDM based on Planck CMB TT, EE, TE likelihood reanalyzed with DES prior [10], we find that the parameter difference tension metric [101] yields a PTE of 0.6 (0.85 σ). The S_8 of $CL + 3 \times 2pt$ is 0.58 σ lower than Planck under ΛCDM as shown in Fig. 9.

Because DES-Y3 CL + 3 × 2pt and Planck CMB are consistent, we combine the two analyses to obtain tighter constraints on the cosmological parameters, which are summarized in Table III. In addition to the improved constraints on S_8 and $\Omega_{\rm m}$, we show the constraints on the sum of neutrino masses in Fig. 10, where the neutrino mass and density Ω_{ν} are related via $\sum m_{\nu} = 93.14\Omega_{\nu}h^2$ eV. As shown in Fig. 10, the DES-Y3 CL + 3 × 2pt is able to break the degeneracy between $\Omega_{\rm m}$ and $\sum m_{\nu}$ in the Planck-only

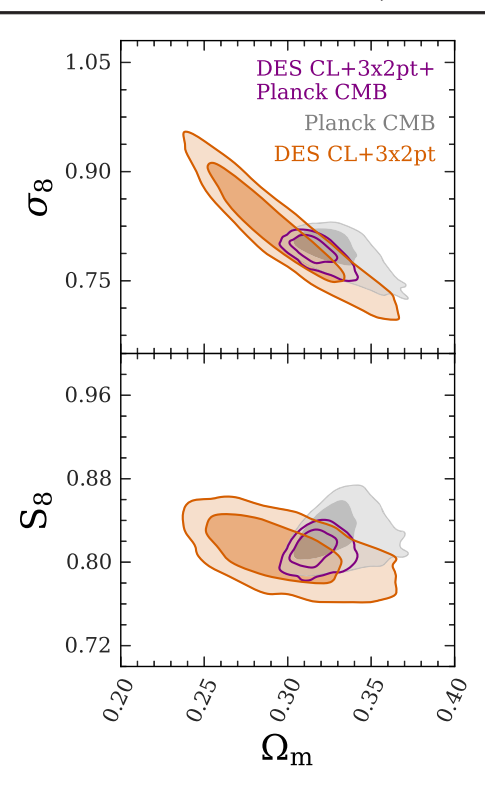


FIG. 9. Marginalized constraints on the three key parameters σ_8 , $S_8 = \sigma_8 \sqrt{\Omega_{\rm m}/0.3}$, and $\Omega_{\rm m}$ in the $\Lambda {\rm CDM}$ model from the joint analysis of DES-Y3 clusters and DES-Y3 3 × 2pt (orange). This measurement is further compared with the predictions from Planck CMB (gray). Given the consistency between different probes, we further show the combined constraints from DES CL + 3 × 2pt and Planck CMB (purple). Contours show 68% and 95% confidence intervals.

constraint. Combining the DES $CL + 3 \times 2pt$ and Planck CMB leads to an upper limit

$$\sum m_{\nu} < 0.26 \text{ eV} \quad (95\%\text{CL}).$$
 (4)

This is a \approx 65% reduction compared to DES-Y3 3 × 2pt + Planck [10] due to a greater constraining power of $\Omega_{\rm m}$. Interestingly, the marginalized posterior of $\sum m_{\nu}$ peaks at 0.1 eV, consistent with the combined constraints of SPT clusters and DES-Y3 3 × 2pt [50].

Finally, we compare the Ω_m constraints from the DES-Y3 CL + 3 × 2pt analysis, DDES-Y3 SN [12], DES-Y6 BAO [36], and DESI-Y1 BAO constraints [13] in Fig. 11. We find that the CL + 3 × 2pt constraints obtain a tighter constraint on Ω_m than 3 × 2pt and pull the value toward DESI BAO constraints. Compared to DES-Y5 SN, the CL + 3 × 2pt obtains an Ω_m value 2.04 σ lower than that of DES-Y5 SN. This is a potentially intriguing deviation—[102] showed that the differences between the Ω_m from DES-Y5 SN and DESI-Y1 BAO under Λ CDM could be due to the evolution of dark energy equation of state. It would be interesting to investigate whether the difference between the Ω_m from DES-Y5 SN and DES-Y6 CL + 3 × 2pt is consistent with the prediction of

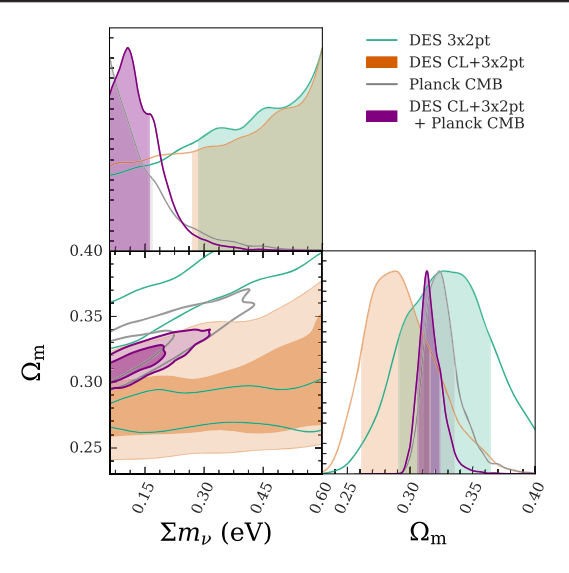


FIG. 10. Marginalized constraints on the sum of neutrino masses $\sum m_{\nu}$ and $\Omega_{\rm m}$ in the $\Lambda{\rm CDM}$ model. We show DES $3\times2{\rm pt}$ (green), DES CL + $3\times2{\rm pt}$ (orange), Planck (gray), and DES CL + $3\times2{\rm pt}$ and Planck CMB (purple). Contours show 68% and 95% confidence intervals. The upper panel shows marginalized posteriors for $\sum m_{\nu}$, with shaded regions showing the 68% confidence interval. The right panel shows marginalized posteriors for $\Omega_{\rm m}$, with shaded regions showing the 68% confidence interval.

the favored $w_0 - w_a$ model in the joint analyses of DESI-Y1 BAO, DES-Y5 SN, and Planck CMB. However, our current model is not validated for the $w_0 - w_a$ model; thus, we leave this investigation to future work.

While we have been focusing on discussions of cosmological parameters, the $CL + 3 \times 2pt$ also provides a stringent constraint on the several nuisance parameters, which are presented in Appendix E. In Appendix D, we further show the inferred mass-richness relation of the DES-Y3 cluster samples based on the $CL + 3 \times 2pt$ analysis and detail the associated calculation.

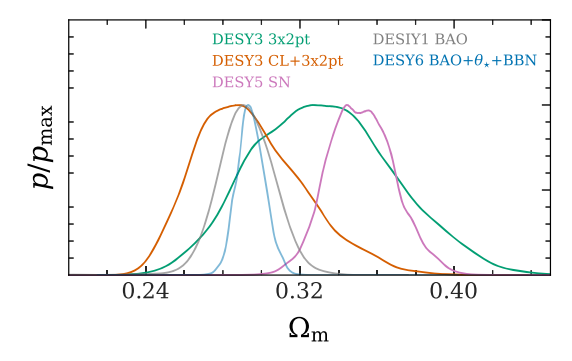


FIG. 11. Marginalized posteriors on $\Omega_{\rm m}$ in the Λ CDM model. We show DES 3×2 pt (green), DES CL + 3×2 pt (orange), DESI-Y1 BAO (gray, [13]), DES-Y6 BAO + θ_{\star} + BBN (blue, [36]) and DES-Y5 supernovae (purple, [12]).

VI. CONCLUSIONS

This work presents the measurement, calibration, and cosmological constraints of cluster abundances and all possible two-point correlation functions between clusters, galaxies, and weak gravitational lensing shears measured in the first three years of DES data. Since DES-Y1 [11], we have improved our analysis framework [58] to meet the accuracy requirement of the much more constraining datasets, which covers about three times the sky area of that of DES-Y1. This improved analysis framework is described in detail and validated to meet the accuracy requirement of the full DES data in [60]. The computationally intensive analysis framework is enabled a customized likelihood inference tool [64] that reduces the computation needs by a factor of 10, making the computation consumptions of the project manageable.

In the first phase of this work, we performed a blinded analysis on the cluster-based data vector (known as the CL + GC analysis): the combination of cluster abundances, cluster lensing, cluster clustering, cluster-galaxy cross-correlation functions, and galaxy clustering. While carrying out the analysis, we shifted key cosmological and nuisance parameters by a random number. This allows us to test the robustness of our analysis and make decisions without knowing the actual cosmological parameters we would obtain. These decisions include the selection-effect model, survey systematics mitigation scheme, cluster lensing scale cuts and the analysis method, the tension metric, and the criteria for the goodness of fit. The blinding and unblinding processes are described in detail in Sec. IV. We do not alter any of the analysis after we unblind.

With~16,000 optically detected clusters, our cluster-based cosmological constraint is the most powerful cosmological constraint from an optically selected cluster sample to date. We have achieved ~50% improvements in the constraints on the key cosmological parameters from our result in DES-Y1. We find that the Λ CDM model is consistent with our cluster-based data vector with constraints on the clustering amplitude $S_8 = 0.864 \pm 0.035$ and matter density $\Omega_{\rm m} = 0.265^{+0.019}_{-0.031}$. Comparing to cluster cosmological constraints in x-ray [47] and SZ [49], we find that our cluster cosmological constraints are consistent with those analyses but have a slight preference for low $\Omega_{\rm m}$ and high S_8 .

Under the Λ CDM model, we find that our cluster cosmology constraint is consistent with the DES-Y3 3 × 2pt constraints presented in [10]. As clusters and DES-Y3 3 × 2pt probe the Universe in different environments and scales, the consistency of the constraints is itself a strong test of the Λ CDM model. Given the consistency of the probes, we then perform a joint analysis of the DES-Y3 cluster and DES-Y3 3 × 2pt, known as the CL + 3 × 2pt analysis. Marginalizing over 41 nuisance parameters, we find constraints on the clustering amplitude

 $S_8=0.811^{+0.022}_{-0.020}$ and matter density $\Omega_{\rm m}=0.294^{+0.022}_{-0.033}$. We have achieved 24% improvements relative to DES-Y3 3 × 2pt on the figure of merit on the $\Omega_{\rm m}$ - S_8 plane, similar to what we found in DES-Y1 [11]. Our S_8 constraint is 0.58σ lower than Planck under Λ CDM, which significantly weakens the claimed S_8 tension from some previous work, where the clustering amplitude measured by low-z measurements tends to be $2-3\sigma$ lower than the prediction of Planck CMB under the Λ CDM model. Our $\Omega_{\rm m}$ is tighter than DES-Y3 3 × 2pt, with the central value pulled toward DESI-BAO, and is $\sim 2\sigma$ lower than that of DES-Y5 SN.

Given the strong consistency between our cosmological constraints and those from Planck CMB, we further combine DES-Y3 CL + 3×2 pt and Planck CMB. We find a mild preference for a nonzero sum of neutrino masses with an upper limit $\sum m_{\nu} < 0.26$ eV [95% confidence interval] under the Λ CDM cosmological model. This is consistent with the findings in the combined analyses of SPT, DES-Y3 3×2 pt and Planck CMB.

This analysis presents the latest joint analyses of galaxy cluster abundances and $3 \times 2pt$ in overlapping surveys, fully accounting for the cross-covariance between different cosmological probes. Our analysis framework has proven to reliably extract cosmological information from galaxy clusters detected in optical surveys and consistently deliver competitive constraints through the two stages of the DES analysis [11]. We note that the analysis framework developed is not only useful for combining optical clusters with $3 \times 2pt$ but also facilitates other combined analyses of clusters and $3 \times 2pt$ [50]. The novel advancement of the modeling and validation plan since DES-Y1 sets the foundation for future low-redshift multiprobe cosmological analyses in Stage-IV lensing surveys such as the Euclid mission, the Vera C. Rubin Observatory's Legacy Survey of Space and Time, and the Nancy Grace Roman Space Telescope.

ACKNOWLEDGMENTS

Funding for the DES Projects has been provided by the U.S. Department of Energy, the U.S. National Science Foundation, the Ministry of Science and Education of Spain, the Science and Technology Facilities Council of the United Kingdom, the Higher Education Funding Council for England, the National Center for Supercomputing Applications at the University of Illinois at Urbana-Champaign, the Kavli Institute of Cosmological Physics at the University of Chicago, the Center for Cosmology and Astro-Particle Physics at the Ohio State University, the Mitchell Institute for Fundamental Physics and Astronomy at Texas A&M University, Financiadora de Estudos e Projetos, Fundação Carlos Chagas Filho de Amparo à Pesquisa do Estado do Rio de Janeiro, Conselho Nacional de Desenvolvimento Científico e Tecnológico and the Ministério da Ciência, Tecnologia e Inovação, the Deutsche Forschungsgemeinschaft and the Collaborating Institutions in the Dark Energy Survey. The collaborating institutions are Argonne National Laboratory, the University of California at Santa Cruz, the University of Cambridge, Centro de Investigaciones Energéticas, Medioambientales y Tecnológicas-Madrid, the University of Chicago, University College London, the DES-Brazil Consortium, the University of Edinburgh, Eidgenössische Technische Hochschule (ETH) Zürich, Fermi National Accelerator Laboratory, the University of Illinois at Urbana-Champaign, the Institut de Ciències de l'Espai (IEEC/CSIC), the Institut de Física d'Altes Energies, Lawrence Berkeley National Laboratory, the Ludwig-Maximilians Universität München and the associated Excellence Cluster Universe, the University of Michigan, NSF NOIRLab, the University of Nottingham, The Ohio State University, the University of Pennsylvania, the University of Portsmouth, SLAC National Accelerator Laboratory, Stanford University, the University of Sussex, Texas A&M University, and the OzDES Membership Consortium. Based in part on observations at NSF Cerro Tololo Inter-American Observatory at NSF NOIRLab (NOIRLab Prop. ID 2012B-0001; PI: J. Frieman), which is managed by the Association of Universities for Research in Astronomy (AURA) under a cooperative agreement with the National Science Foundation. The DES data management system is supported by the National Science Foundation under Grants No. AST-1138766 and No. AST-1536171. The DES participants from Spanish institutions are partially supported by MICINN under Grants No. PID2021-123012, No. PID2021-128989, PID2022-141079, SEV-2016-0588, No. No. No. CEX2020-001058-M and No. CEX2020-001007-S, some of which include ERDF funds from the European Union. IFAE is partially funded by the CERCA program of the Generalitat de Catalunya. We acknowledge support from the Brazilian Instituto Nacional de Ciência e Tecnologia (INCT) do e-Universo (CNPq Grant No. 465376/2014-2). This document was prepared by the DES Collaboration using the resources of the Fermi National Accelerator Laboratory (Fermilab), a U.S. Department of Energy, Office of Science, Office of High Energy Physics HEP User Facility. Fermilab is managed by Fermi Forward Discovery Group, LLC, acting under Contract No. 89243024CSC000002. We would like to thank Stanford University, the Stanford Research Computing Center, the Ohio Supercomputer Center, and the University of Chicago's Research Computing Center for providing the computational resources and support that contributed to these research results.

All authors contributed to this paper and/or carried out infrastructure work that made this analysis possible. Some highlighted contributions from the authors of this paper include: *Scientific management and coordination*: Chun-Hao To and Matteo Costanzi (Cluster working group conveners). *Significant contributions to project*

development, including paper writing and figures: C. C., E. K., C.-H. T., and H.-Y. W. Data analysis and methods validation: E. K., E. R., C.-H. T., H.-Y. W., and R. H. W. Data vector generation: C.-H. T. Internal reviewers: J. B. (Model and validation), S. B. (Model and validation), A. F., T. J., and Y. Z. Advising: D. H. W. The remaining authors have made contributions to this paper that include, but are not limited to, the construction of DECam and other aspects of collecting the data; data processing and calibration; developing broadly used methods, codes, and simulations; running the pipelines and validation tests; and promoting the science analysis.

DATA AVAILABILITY

The data that support the findings of this article are openly available [103]; embargo periods may apply.

APPENDIX A: CATALOG UPDATE FROM [10]

After the publication of [10], it was discovered that there was an inconsistency between the tomographic binning of the source catalog used for the data vector measurements and the redshift distribution used for the cosmological inference. The updated catalog has since been used by [104].

In this work, since we would like to combine the cluster probes with the $2 \times 2pt$ probes, we also present the updated cosmological constraints to [10] using the corrected source catalog. Figure 12 compares the constraints from [10] (black) and the updated data vectors running through the same analysis pipeline (red). We find that the updated

constraints shift a negligible amount $(0.11\sigma \text{ in } \Omega_{\text{m}} \text{ and } 0.32\sigma \text{ in } S_8)$ from the published results, demonstrating that the cosmological constraints from [10] remain robust. Interestingly, though perhaps expected, the new constraints also have a much better goodness of fit, going from a p value of 0.07 to 0.47.

To facilitate the connection of this work with the published results in [10], in Fig. 12, we plot again the updated constraint and compare with the constraints using the same data vector but analysis pipeline adopted by this work (see Sec. III and [60]) implemented both via CosmoSIS and CosmoLike. We find that CosmoSIS and CosmoLike give consistent cosmological constraints $(0.07\sigma$ in $\Omega_{\rm m}$ and 0.2σ in S_8), while CosmoLike is somewhat broader than that of CosmoSIS. Given that the two analyses use sufficiently different samplers and modeling codes, this level of discrepancy is expected. We further compare the difference between CosmoSIS and CosmoLike predictions and find a difference of $\Delta \chi = 0.20$ for 3×2 pt and $\Delta \chi^2 = 0.06$ for 2×2 pt, similar to the findings in [105].

APPENDIX B: DATA VECTORS

We show in Figs. 13–17 the full set of data vectors used in this work. For all figures, each panel shows the data points in the upper part and the fractional difference between the data and the mean of the predictions from the CL + GC chains, normalized by the PPD prediction scatter (Appendix C). Data points excluded from the analysis by scale cuts are shown in light opacity.

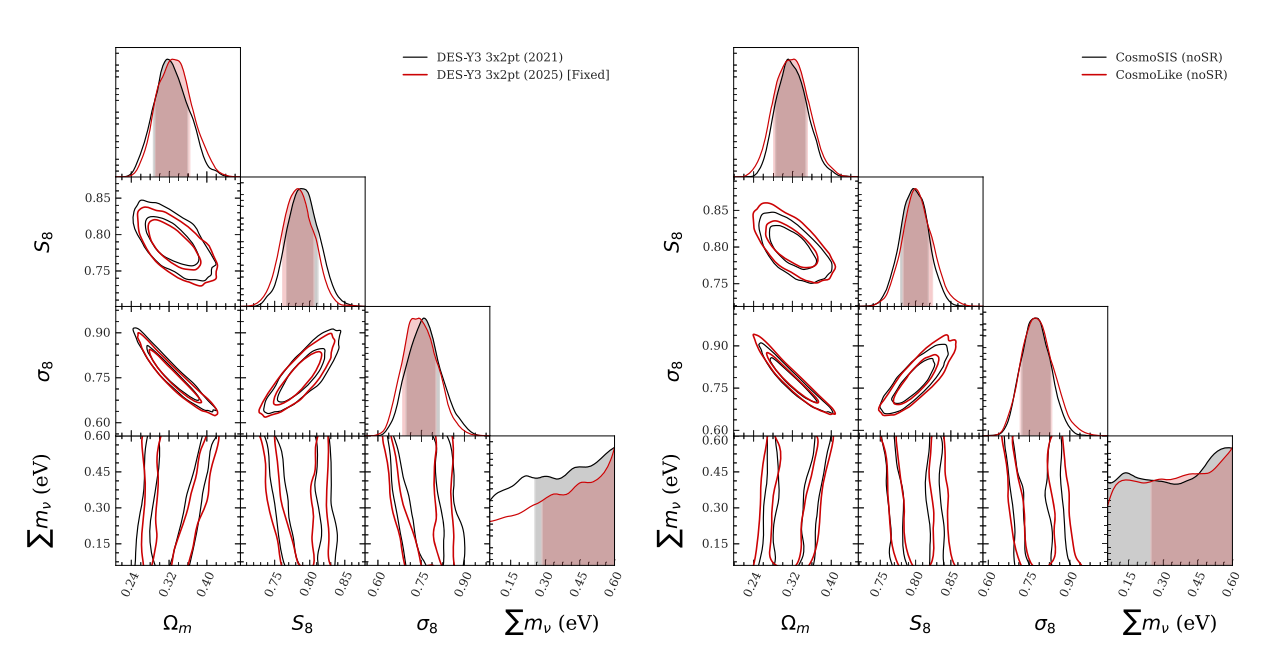


FIG. 12. Left: Comparison of the $3 \times 2pt$ cosmological constraints from [10] (black) and the same inference pipeline with the updated shear catalog (red). Right: Comparison of the updated $3 \times 2pt$ constraints using inference pipeline in [10] and that used in this work, implemented through both CosmoSIS (black) and CosmoLike (red).

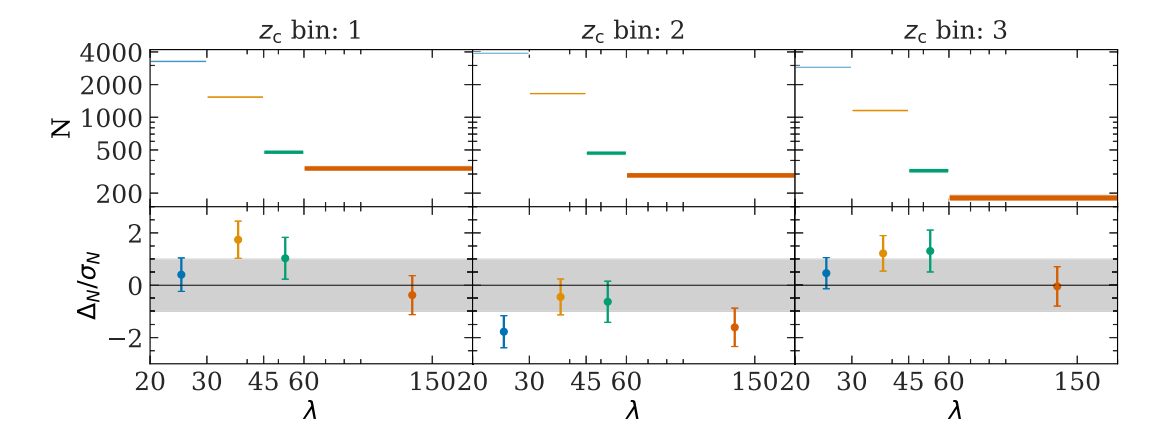


FIG. 13. Measured cluster abundances for each tomographic bin. Each panel in column i corresponds to measurements using redMaPPer clusters in tomographic bin i. The shaded region represents 1σ uncertainties. The lower part of each panel shows fractional differences between the data and the mean prediction from the CL + GC chains, normalized by the prediction scatter. Shaded bands denote the 1σ confidence interval.

APPENDIX C: POSTERIOR PREDICTIVE DISTRIBUTION (PPD)

Here, we briefly summarize the PPD calculation. We refer the readers to [99] for a more in-depth description and only focus on the differences in this section. Throughout the paper, we have used PPD for two purposes:

- (1) To quantify the goodness of fit between model (M) and data (d).
- (2) To quantify the consistency between two data vectors $(\mathbf{d}_1 \text{ and } \mathbf{d})$, given a model (\mathbf{M}) .

To carry out these two calculations, we need to evaluate two probabilities $P(\mathbf{d}|\mathbf{M})$ and $P(\mathbf{d}|\mathbf{d}_1,\mathbf{M})$, respectively. We approximate each probability as a Gaussian Mixture Model, written as

$$P(\mathbf{d}|\mathbf{d}_{1}, \mathbf{M}) = \sum_{i} \phi^{i} Gauss(\mathbf{d} - \boldsymbol{\mu}_{2,i} - \mathbf{C}_{21}^{-1} \mathbf{C}_{11}^{-1} (\mathbf{d}_{1} - \boldsymbol{\mu}_{1,i}),$$

$$\mathbf{C}_{22} - \mathbf{C}_{21} \mathbf{C}_{11}^{-1} \mathbf{C}_{12}), \tag{C1}$$

$$P(\mathbf{d}|\mathbf{M}) = \sum_{i} \phi^{i} \operatorname{Gauss}(\mathbf{d} - \boldsymbol{\mu}_{i}, \mathbf{C}), \tag{C2}$$

where *i* runs over the steps of the MCMC chains, ϕ^i are arbitrary normalization constants, Gauss(\mathbf{x}, \mathbf{y}) denotes a multivariate Gaussian distribution with mean \mathbf{x} and covariance \mathbf{y} , \mathbf{C} is the covariance matrix of the data vector, and $\mathbf{C}_{\mathbf{x}_1,\mathbf{x}_2}$ is the covariance matrix between data vector \mathbf{x}_1 and \mathbf{x}_2 . In the above expression, $\boldsymbol{\mu}_i$ is the theory prediction at step *i* of the MCMC chain. For simplicity, we use $P(\mathbf{d}, \mathbf{M})$ to denote $P(\mathbf{d}|\mathbf{d}_1, \mathbf{M})$ when testing the consistency of data and $P(\mathbf{d}|\mathbf{M})$ when testing the goodness of fit of the model.

To evaluate the consistency or the goodness of fit, we need to estimate whether the data at hand (\mathbf{d}_o) is consistent with a random draw from the $P(\mathbf{d}, \mathbf{M})$. We calculate the posterior predictive distribution (PPD) defined as

$$PPD(\mathbf{d}_o|\mathbf{M}) := P(P(\mathbf{d}_o|\mathbf{M}) > P(\mathbf{d}_r|\mathbf{M}))$$
 (C3)

$$PPD(\mathbf{d}_o|\mathbf{d}_1, \mathbf{M}) := P(P(\mathbf{d}_o|\mathbf{d}_1, \mathbf{M}) > P(\mathbf{d}_r|\mathbf{d}_1, \mathbf{M})), \quad (C4)$$

where \mathbf{d}_r is a random sample from $P(\mathbf{d}|\mathbf{M})$ in Eq. (C2) and from $P(\mathbf{d}|\mathbf{d}_1,\mathbf{M})$ in Eq. (C1). We numerically calculate the above probability with 15,000 random draws from $P(\mathbf{d},\mathbf{M})$. A low PPD value indicates that the data at hand is not a random draw from $P(\mathbf{d}|\mathbf{M})$, while a high PPD value could indicate a problem in the model, such as an overestimation of the covariance matrix.

Finally, with a large number of draws, $P(\mathbf{d}_r)$ can be approximated as a Gaussian distribution. We can evaluate the mean and the standard deviation from the $P(\mathbf{d}_r)$ and compare it with the data vector at hand \mathbf{d}_o . While less accurate, this comparison can be used as a visual check on whether the data and model are compatible. We plot this comparison in the lower panel of Figs. 13–17 and do not find any obvious deviation.

APPENDIX D: MASS-OBSERVABLE RELATIONS

We calculate the mass distribution of our samples using the posterior from the $CL + 3 \times 2pt$ analysis. Specifically, the mass distribution of a cluster given a richness bin $\Delta \lambda_c$ at redshift z can be calculated as

$$P(M|\Delta\lambda, z) = \frac{\int_{\lambda \in \Delta\lambda_c} n(M, z) P(\lambda|M, z) d\lambda}{\int_{\lambda \in \Delta\lambda} n(M, z) d\lambda}, \quad (D1)$$

where n(M,z) is the halo mass function, and $P(\lambda|M,z)$ is the richness-mass relation. The mass distribution of redMaPPer is shown in Fig. 18. We further show comparison with SPT-Pol [106] and eRASS1 [47]. To facilitate the comparison, we use the COLOSSUS [107] package to convert $M_{500~\rm C}$ to $M_{200~\rm m}$ and assume an NFW profile with a concentraion-mass relation [108].

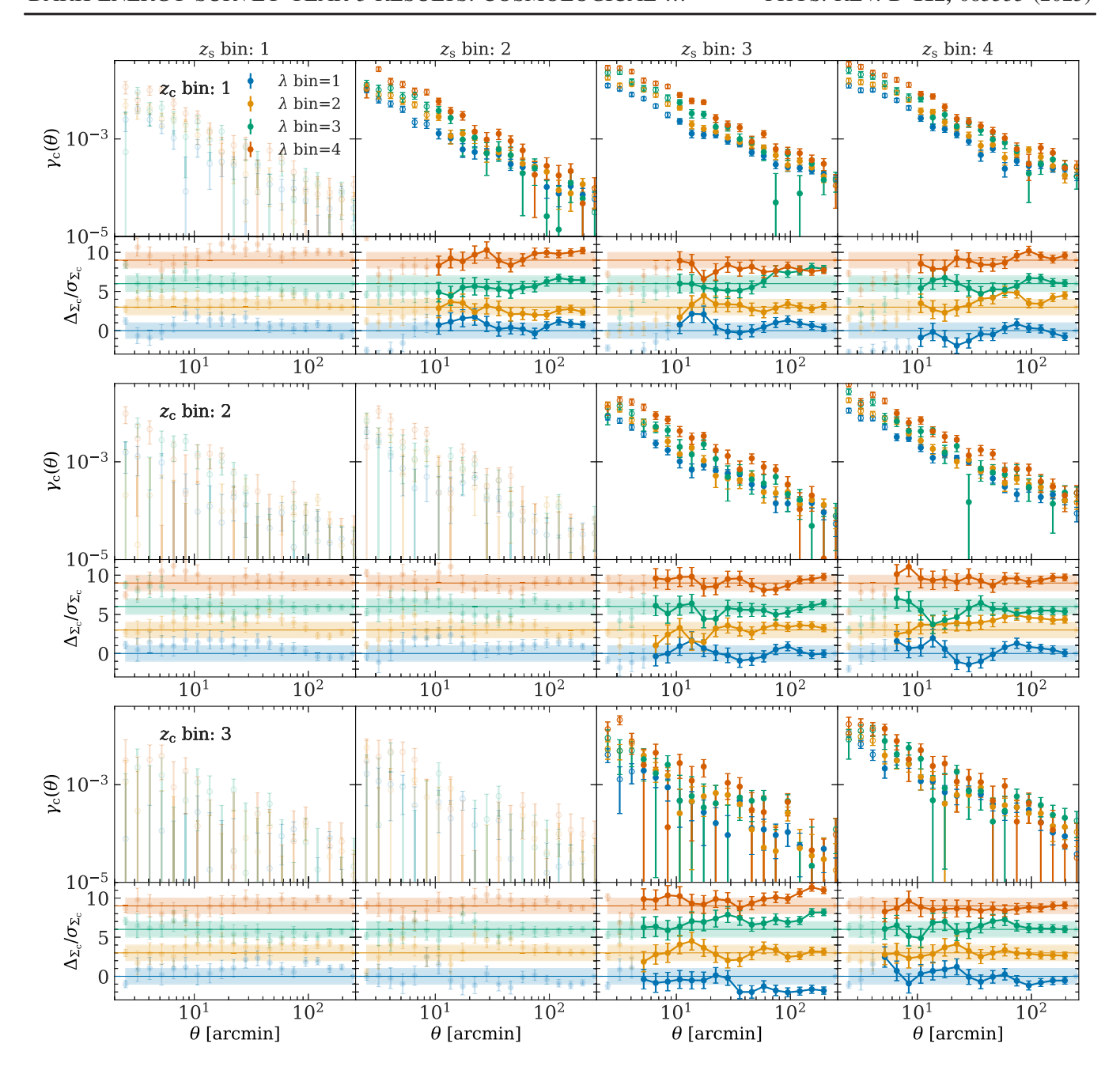


FIG. 14. Measured γ_c correlation functions for each tomographic bin combination. Each panel in row i and column j represents the measurement using clusters from tomographic bin i and source galaxies from tomographic bin j. Colors indicate different richness bins, with error bars denoting 1σ uncertainties. Faint dots indicate data points excluded from the analysis. The lower part of each panel shows the fractional differences between the data and the mean of the predictions from the CL + GC chains, normalized by the prediction scatter. For clarity, each richness bin is artificially shifted by 3. Shaded bands represent the 1σ confidence interval.

Further, the $CL + 3 \times 2pt$ leads to a stringent constraint on the mean halo mass-richness relation. Marginalized over cosmological and nuisance parameters, the mean mass of redMaPPer clusters is constrained as

$$\langle M_{\rm 200~m} | \lambda \rangle = 10^{14.399 \pm 0.011} \left(\frac{\lambda}{40} \right)^{1.053 \pm 0.031} \left(\frac{1+z_{\lambda}}{1.45} \right)^{-0.667 \pm 0.194} h^{-1} M_{\odot}.$$

Since the richness changes between DES-Y1 and DES-Y3 (Fig. 3), it is hard to compare this value with existing literature. However, we note that while the normalization changes, we find that the constrained slope of the mass-richness relation is consistent with those in the literature [11,109].

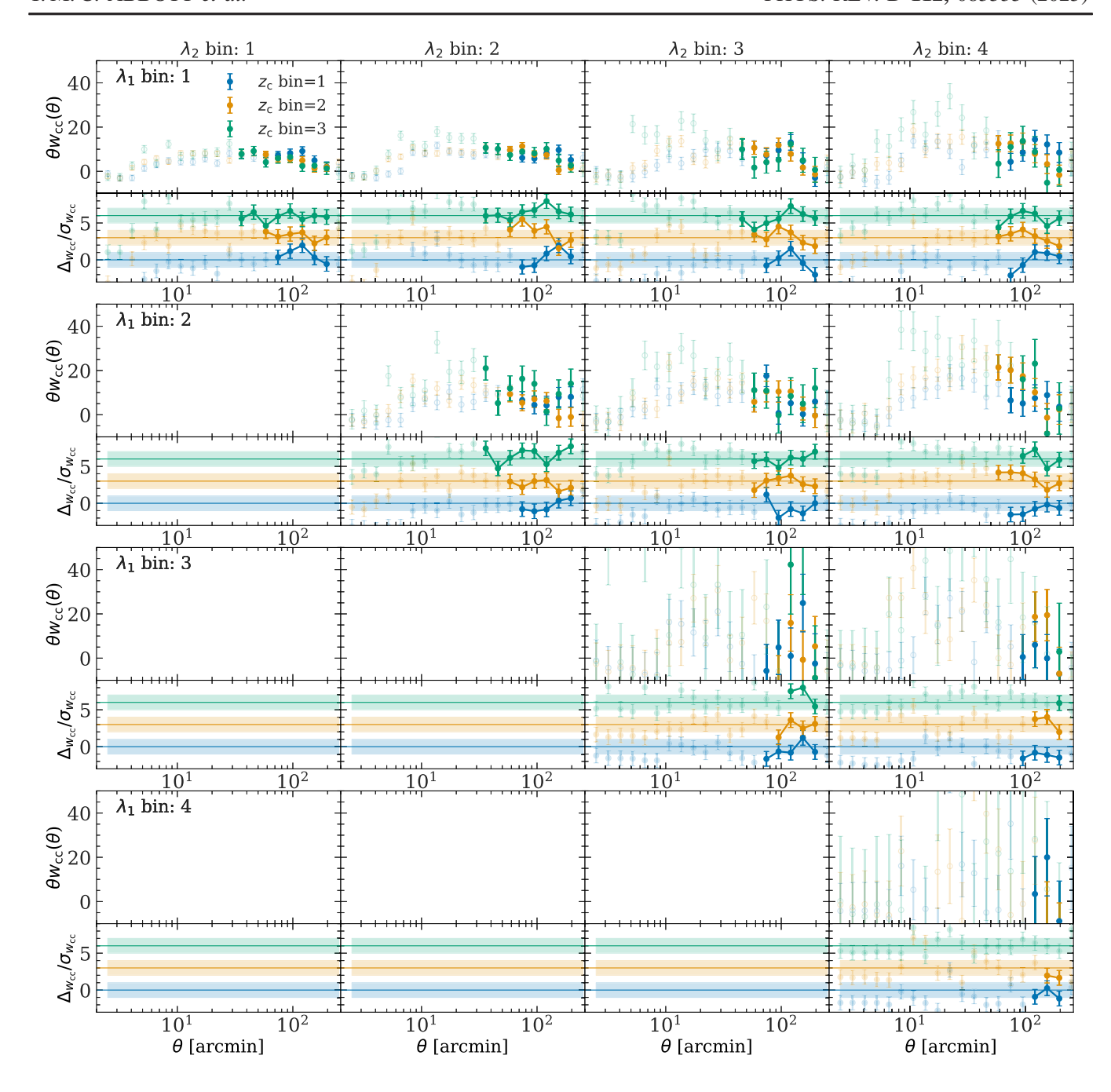


FIG. 15. Measured w_{cc} correlation functions for each tomographic and richness bin combination. Each panel in row i and column j represents the measurement using clusters with richness i and clusters with richness j. Colors indicate different redshift bins, with error bars denoting 1σ uncertainties. Faint dots indicate data points excluded from the analysis. The lower part of each panel shows the fractional differences between the data and the mean of the predictions from the CL + GC chains, normalized by the prediction scatter. For clarity, each richness bin is artificially shifted by 3. Shaded bands represent the 1σ confidence interval.

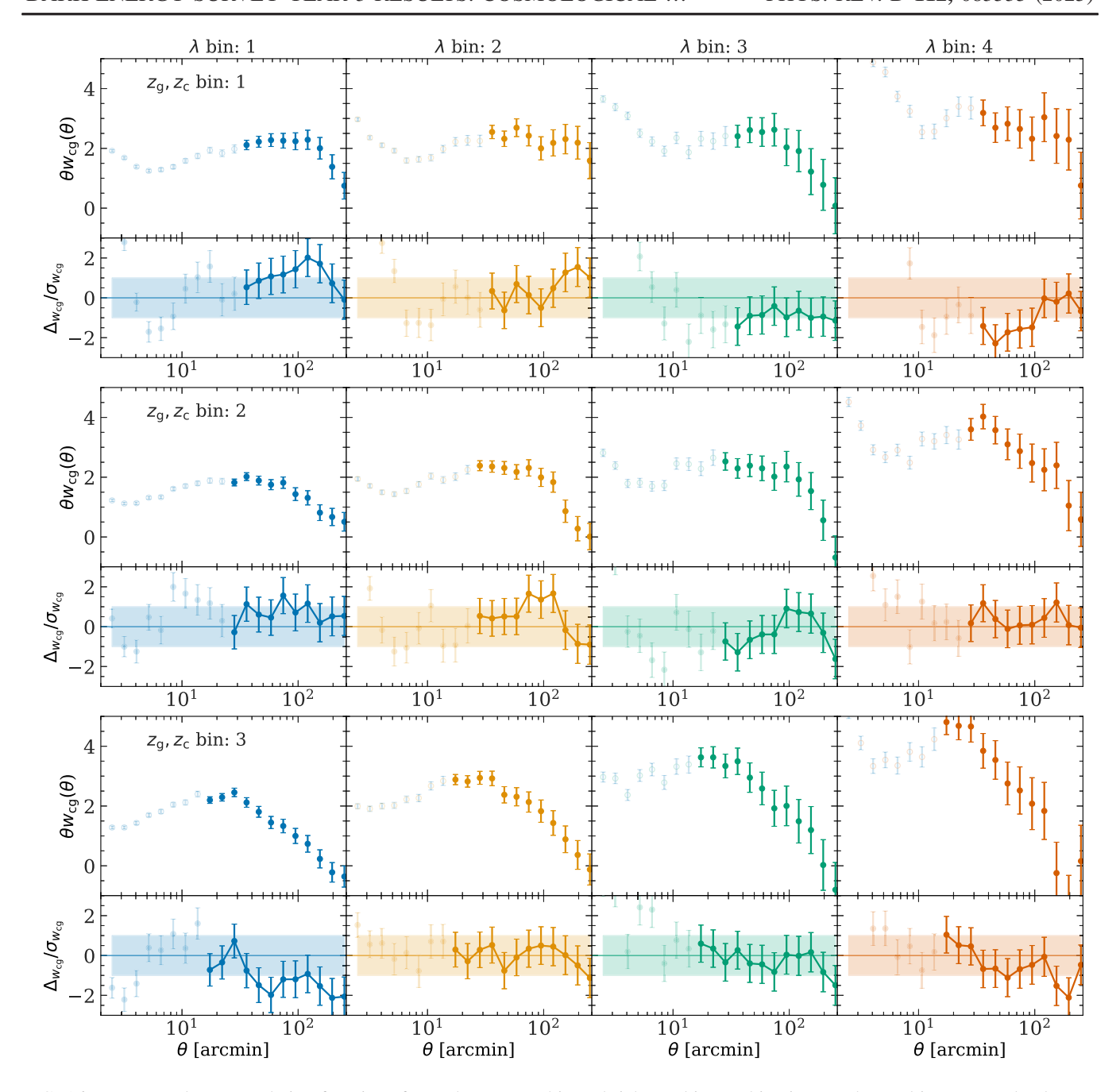


FIG. 16. Measured $w_{\rm cg}$ correlation functions for each tomographic and richness bin combination. Each panel in row i and column j represents the measurement using clusters from tomographic bin i with richness j and Maglim galaxies from tomographic bin i. Colors indicate different richness bins, with error bars denoting 1σ uncertainties. Faint dots indicate data points excluded from the analysis. The lower part of each panel shows the fractional differences between the data and the mean of the predictions from the CL + GC chains, normalized by the prediction scatter. For clarity, each richness bin is artificially shifted by 3. Shaded bands represent the 1σ confidence interval.

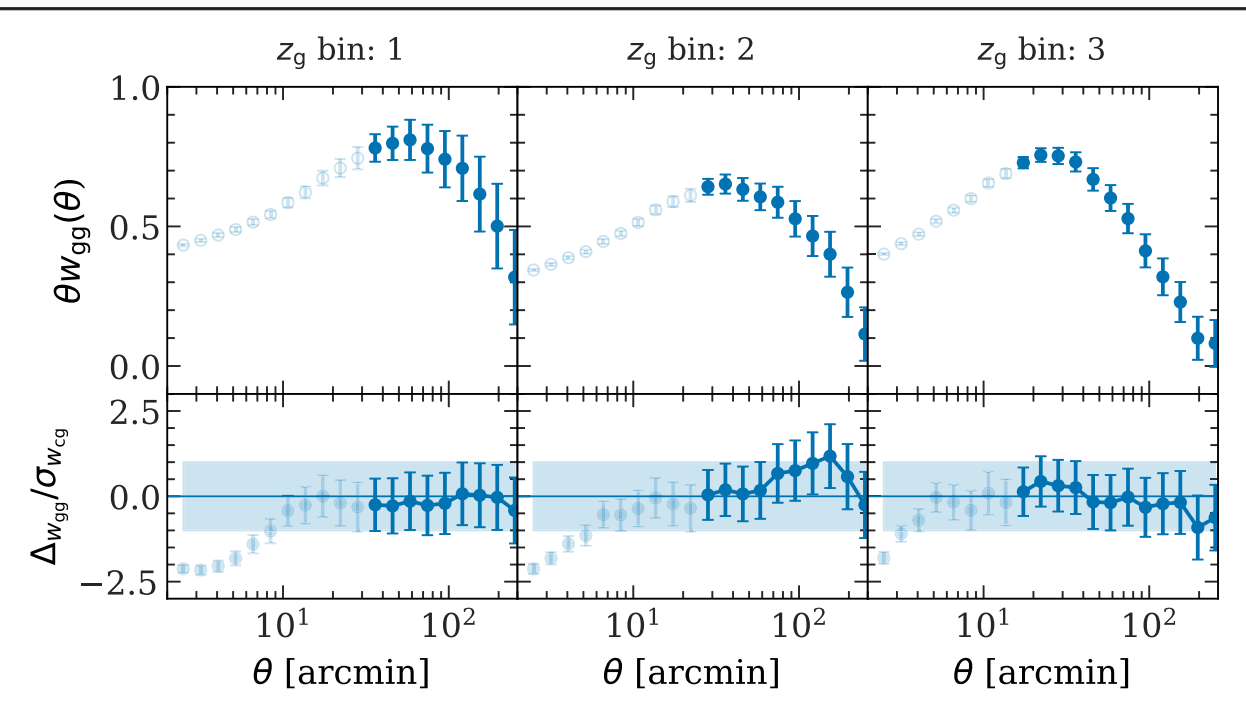


FIG. 17. Measured w_{gg} correlation functions for each tomographic bin. Each panel in column i corresponds to measurements using Maglim galaxies in tomographic bin i. Error bars represent 1σ uncertainties, with faint dots indicating data points excluded from the analysis. The lower part of each panel shows fractional differences between the data and the mean prediction from the CL + GC chains, normalized by the prediction scatter. For clarity, each richness bin is offset by 3. Shaded bands denote the 1σ confidence interval.

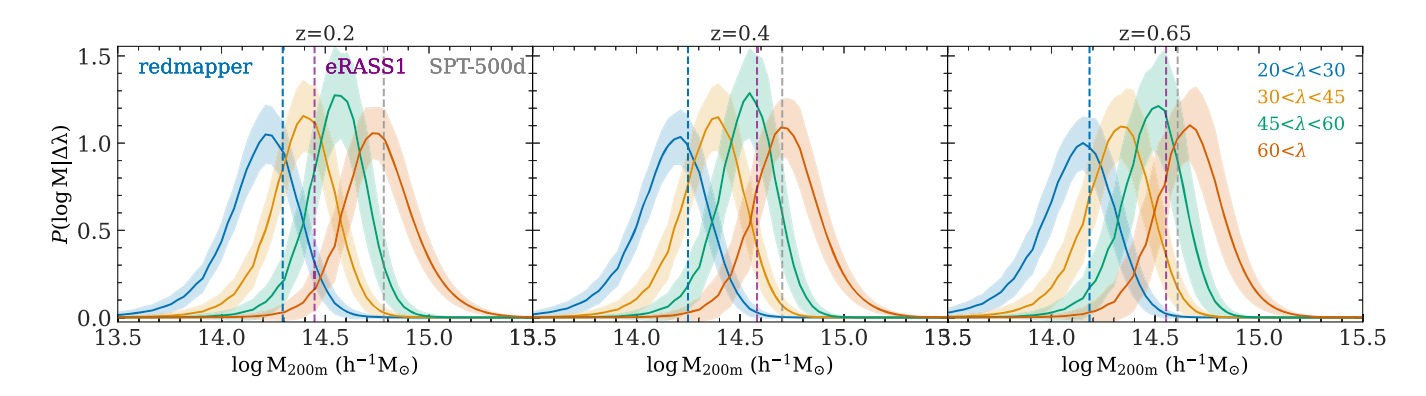


FIG. 18. Distribution of redMaPPer cluster mass in each richness bin. The width of the bands corresponds to the 68% confidence interval of the distribution sampled from the posterior of the $CL + 3 \times 2pt$ analysis. Dashed lines show median mass of the samples in each redshift, including redMaPPer (blue), eRASS1 (purple), SPTpol (gray).

APPENDIX E: ALL PARAMETERS

We show constraints of nuisance parameters in Fig. 19. The one-dimensional mean and 1σ confidence intervals of the nuisance parameters are summarized in Table IV. Interestingly, we find that the selection bias is consistent with 1, indicating no detection of selection effect on large scales. This is consistent with our findings in DES-Y1 [11].

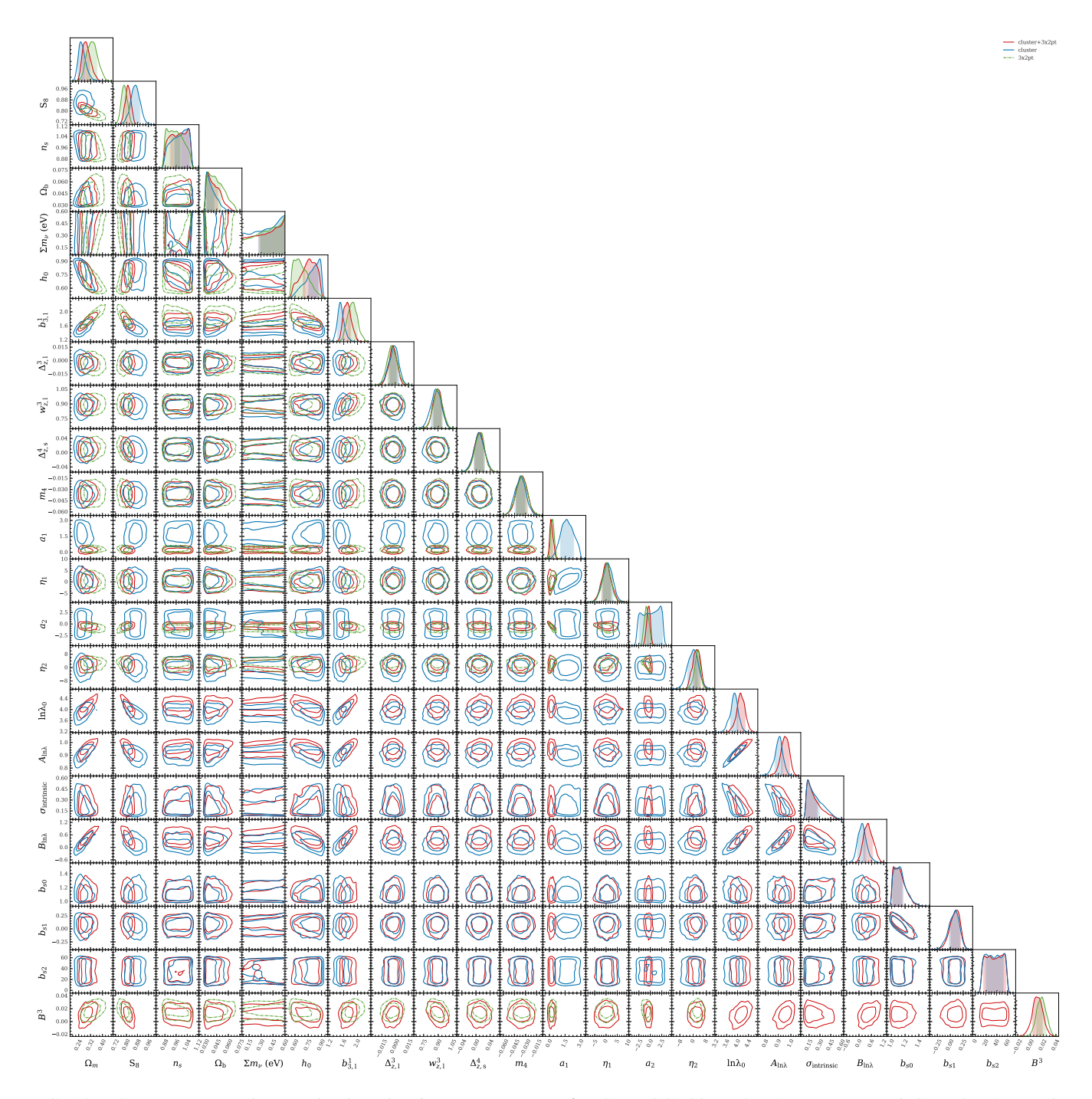


FIG. 19. Summary cosmology and selected nuisance parameters for CL + GC (blue), $3 \times 2pt$ (green), and $CL + 3 \times 2pt$ (red). Contours show 68% and 95% confidence intervals. For lens galaxies, we only show parameters related to the third Maglim bin, which is the highest redshift bin for CL + GC analysis. For source galaxies, we show parameters related to the fourth Metacalibration bin.

TABLE IV. Summary of the mean and 1σ confidence interval of the nuisance parameters constrained by CL+GC and $CL+3\times 2pt$. Parameters that are not constrained are indicated by a center dots.

Parameter	$CL + 3 \times 2pt$	CL + GC	
Galaxy bias			
$b_{1,1}^{1}$	$1.194^{+0.068}_{-0.094}$	$1.356^{+0.083}_{-0.100}$	
$b_{1,1}^{2}$	$1.494^{+0.081}_{-0.120}$	$1.562^{+0.090}_{-0.120}$	
$b_{1,1}^{3}$	$1.519_{-0.110}^{+0.085}$	$1.709_{-0.130}^{+0.093}$	
$b_{1,1}^{4}$	• • •	$1.630^{+0.100}_{-0.120}$	
Intrinsic alignm	ent		
a_1	1.717 ± 0.604	$0.203^{+0.143}_{-0.189}$	
η_1	0.735 ± 2.346	0.255 ± 2.276	
a_2	• • •	$-0.403^{+0.435}_{-0.374}$	
η_2	• • •	$2.020^{+2.640}_{-2.089}$	
Point-mass mar	ginalization		
B^0	•••	$0.008^{+0.007}_{-0.007}$	
B^1		-0.001 ± 0.008	
B^2	•••	0.011 ± 0.009	
B^3	• • •	0.006 ± 0.010	
redMaPPer richness-mass relation			
$\ln \lambda_0$	$3.874^{+0.167}_{-0.136}$	$4.122^{+0.162}_{-0.146}$	
$A_{\ln \lambda}$	$0.903^{+0.037}_{-0.029}$	$0.953^{+0.037}_{-0.030}$	
$B_{\ln \lambda}$	$0.163^{+0.183}_{-0.245}$	$0.462^{+0.209}_{-0.263}$	
$\sigma_{ m intrinsic}$	$0.238^{+0.053}_{-0.140}$	$0.222^{+0.041}_{-0.120}$	
redMaPPer se	lection effect		
b_{s1}	$1.128^{+0.044}_{-0.110}$	$1.123^{+0.043}_{-0.110}$	
b_{s2}	$0.067^{+0.120}_{-0.089}$	$0.086^{+0.110}_{-0.084}$	
r_0			

APPENDIX F: COMPARISONS WITH PREVIOUS DES CLUSTER ANALYSES

Figure 20 compares DES cluster cosmology analyses. The comparison of the large-scale-based analysis between DES-Y1 and DES-Y3 was discussed in Sec. IV B. Specifically, the analysis of Y3 data with Y1 cluster lensing analysis choices shifts the contour toward DES-Y1 constraints. However, we believe that Y1 cluster lensing analysis has residual contaminations from small-scale cluster lensing due to the lensing estimator being nonlocal. We decided to adopt the Y3 analysis choice as fiducial before we unblind the parameter constraints. As a comparison, we also show constraints from DES-Y1 cluster

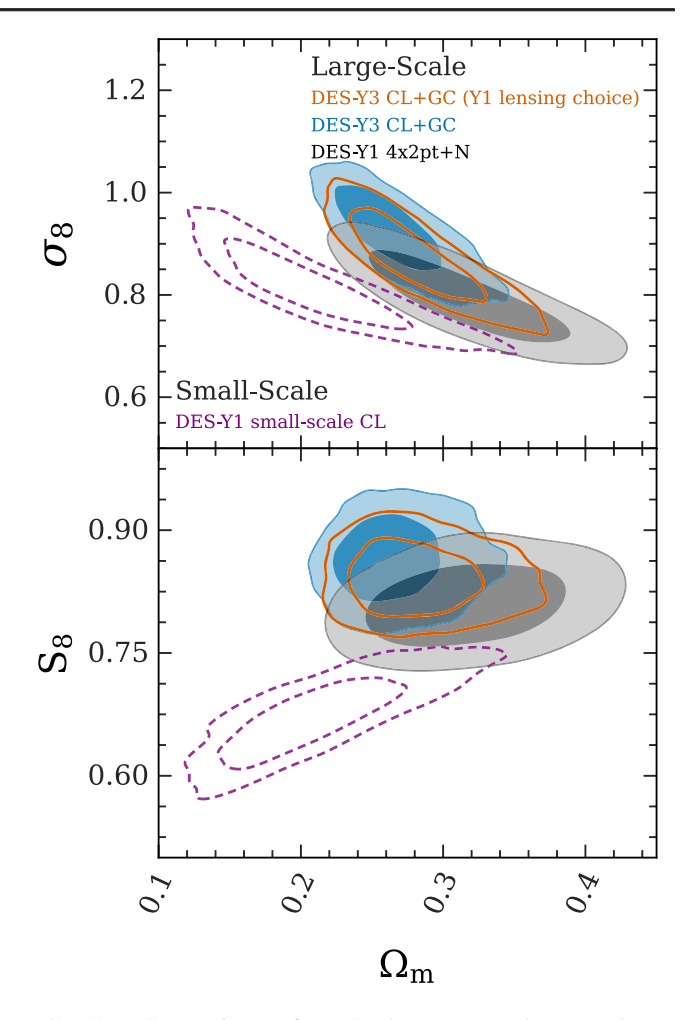


FIG. 20. Comparison of DES cluster cosmology analyses, including DES-Y3 CL + GC analysis (blue), DES-Y3 CL + GC analysis with Y1 lensing analyses choices (orange), and DES-Y1 CL + GC analysis (gray, [11]). We further compare with the analysis based on small-scale cluster lensing and cluster abundances (purple, [70]).

analyses using small-scale cluster lensing information, presented in [70]. These constraints differ slightly from the fiducial constraints presented in [57], with a 0.5σ shift in the Ω_m - σ_8 plane, which is due to differences in the sampling methods and the adopted richness-mass relations. The DES-Y1 cluster analyses using small-scale cluster lensing are known to be affected by selection effects [57,109] and are inconsistent with the large-scale analyses.

^[1] A. G. Riess, A. V. Filippenko, P. Challis, A. Clocchiatti, A. Diercks, P. M. Garnavich, R. L. Gilliland, C. J. Hogan, S. Jha, R. P. Kirshner *et al.*, Astron. J. **116**, 1009 (1998).

^[2] S. Perlmutter, G. Aldering, G. Goldhaber, R. A. Knop, P. Nugent, P. G. Castro, S. Deustua, S. Fabbro, A. Goobar, D. E. Groom *et al.*, Astrophys. J. **517**, 565 (1999).

- [3] N. Suzuki, D. Rubin, C. Lidman, G. Aldering, R. Amanullah, K. Barbary, L. F. Barrientos, J. Botyanszki, M. Brodwin, N. Connolly *et al.*, Astrophys. J. **746**, 85 (2012).
- [4] G. Hinshaw, D. Larson, E. Komatsu, D. N. Spergel, C. L. Bennett, J. Dunkley, M. R. Nolta, M. Halpern, R. S. Hill, N. Odegard *et al.*, Astrophys. J. Suppl. Ser. 208, 19 (2013).
- [5] M. Betoule, R. Kessler, J. Guy, J. Mosher, D. Hardin, R. Biswas, P. Astier, P. El-Hage, M. Konig, S. Kuhlmann *et al.*, Astron. Astrophys. **568**, A22 (2014).
- [6] S. Alam, M. Ata, S. Bailey, F. Beutler, D. Bizyaev, J. A. Blazek, A. S. Bolton, J. R. Brownstein, A. Burden, C.-H. Chuang *et al.*, Mon. Not. R. Astron. Soc. **470**, 2617 (2017).
- [7] D. M. Scolnic, D. O. Jones, A. Rest, Y. C. Pan, R. Chornock, R. J. Foley, M. E. Huber, R. Kessler, G. Narayan, A. G. Riess et al., Astrophys. J. 859, 101 (2018).
- [8] N. Aghanim, Y. Akrami, M. Ashdown, J. Aumont, C. Baccigalupi, M. Ballardini, A. J. Banday, R. B. Barreiro, N. Bartolo *et al.* (Planck Collaboration), Astron. Astrophys. 641, A6 (2020).
- [9] T. M. C. Abbott, F. B. Abdalla, A. Alarcon, J. Aleksić, S. Allam, S. Allen, A. Amara, J. Annis, J. Asorey, S. Avila et al., Phys. Rev. D 98, 043526 (2018).
- [10] T. M. C. Abbott, M. Aguena, A. Alarcon, S. Allam, O. Alves, A. Amon, F. Andrade-Oliveira, J. Annis, S. Avila, D. Bacon *et al.*, Phys. Rev. D **105**, 023520 (2022).
- [11] C. To, E. Krause, E. Rozo, H. Wu, D. Gruen, R. H. Wechsler, T. F. Eifler, E. S. Rykoff, M. Costanzi, M. R. Becker *et al.*, Phys. Rev. Lett. **126**, 141301 (2021).
- [12] T. M. C. Abbott, M. Acevedo, M. Aguena, A. Alarcon, S. Allam, O. Alves, A. Amon, F. Andrade-Oliveira, J. Annis et al. (DES Collaboration), Astrophys. J. Lett. 973, L14 (2024).
- [13] A. G. Adame, J. Aguilar, S. Ahlen, S. Alam, D. M. Alexander, M. Alvarez, O. Alves, A. Anand, U. Andrade *et al.* (DESI Collaboration), arXiv:2404.03002.
- [14] A. G. Adame, J. Aguilar, S. Ahlen, S. Alam, D. M. Alexander, C. Allende Prieto, M. Alvarez, O. Alves, A. Anand *et al.* (DESI Collaboration), J. Cosmol. Astropart. Phys. 07 (2025) 028.
- [15] J. A. Frieman, M. S. Turner, and D. Huterer, Annu. Rev. Astron. Astrophys. 46, 385 (2008).
- [16] D. H. Weinberg, M. J. Mortonson, D. J. Eisenstein, C. Hirata, A. G. Riess, and E. Rozo, Phys. Rep. 530, 87 (2013).
- [17] D. Huterer, D. Kirkby, R. Bean, A. Connolly, K. Dawson, S. Dodelson, A. Evrard, B. Jain, M. Jarvis, E. Linder *et al.*, Astropart. Phys., **63**, 23 (2015).
- [18] M. S. Turner, Annu. Rev. Nucl. Part. Sci. 72, 1 (2022).
- [19] D. Huterer, Astron. Astrophys. Rev. 31, 2 (2023).
- [20] C. Hikage, M. Oguri, T. Hamana, S. More, R. Mandelbaum, M. Takada, F. Köhlinger, H. Miyatake, A. J. Nishizawa, H. Aihara *et al.*, Publ. Astron. Soc. Jpn. 71, 43 (2019).
- [21] T. Hamana, M. Shirasaki, S. Miyazaki, C. Hikage, M. Oguri, S. More, R. Armstrong, A. Leauthaud, R. Mandelbaum, H. Miyatake *et al.*, Publ. Astron. Soc. Jpn. 72, 16 (2020).
- [22] C. Heymans, T. Tröster, M. Asgari, C. Blake, H. Hildebrandt, B. Joachimi, K. Kuijken, C.-A. Lin, A. G.

- Sánchez, J. L. van den Busch *et al.*, Astron. Astrophys. **646**, A140 (2021).
- [23] M. Asgari, C.-A. Lin, B. Joachimi, B. Giblin, C. Heymans, H. Hildebrandt, A. Kannawadi, B. Stölzner, T. Tröster, J. L. van den Busch *et al.*, Astron. Astrophys. **645**, A104 (2021).
- [24] L. F. Secco, S. Samuroff, E. Krause, B. Jain, J. Blazek, M. Raveri, A. Campos, A. Amon, A. Chen, C. Doux *et al.*, Phys. Rev. D **105**, 023515 (2022).
- [25] A. Amon, D. Gruen, M. A. Troxel, N. MacCrann, S. Dodelson, A. Choi, C. Doux, L. F. Secco, S. Samuroff, E. Krause *et al.*, Phys. Rev. D **105**, 023514 (2022).
- [26] R. Dalal, X. Li, A. Nicola, J. Zuntz, M. A. Strauss, S. Sugiyama, T. Zhang, M. M. Rau, R. Mandelbaum, M. Takada *et al.*, Phys. Rev. D **108**, 123519 (2023).
- [27] X. Li, T. Zhang, S. Sugiyama, R. Dalal, R. Terasawa, M. M. Rau, R. Mandelbaum, M. Takada, S. More, M. A. Strauss *et al.*, Phys. Rev. D **108**, 123518 (2023).
- [28] E. Di Valentino, L. A. Anchordoqui, Ö. Akarsu, Y. Ali-Haimoud, L. Amendola, N. Arendse, M. Asgari, M. Ballardini, S. Basilakos, E. Battistelli *et al.*, Astropart. Phys. 131, 102604 (2021).
- [29] L. Perivolaropoulos and F. Skara, New Astron. Rev. 95, 101659 (2022).
- [30] E. Abdalla, G. F. Abellán, A. Aboubrahim, A. Agnello, Ö. Akarsu, Y. Akrami, G. Alestas, D. Aloni, L. Amendola, L. A. Anchordoqui *et al.*, J. High Energy Astrophys. 34, 49 (2022).
- [31] A. Amon and G. Efstathiou, Mon. Not. R. Astron. Soc. **516**, 5355 (2022).
- [32] C. Preston, A. Amon, and G. Efstathiou, Mon. Not. R. Astron. Soc. 525, 5554 (2023).
- [33] K. K. Rogers, R. Hložek, A. Laguë, M. M. Ivanov, O. H. E. Philcox, G. Cabass, K. Akitsu, and D. J. E. Marsh, J. Cosmol. Astropart. Phys. 06 (2023) 023.
- [34] D. W. Pesce, J. A. Braatz, M. J. Reid, A. G. Riess, D. Scolnic, J. J. Condon, F. Gao, C. Henkel, C. M. V. Impellizzeri, C. Y. Kuo *et al.*, Astrophys. J. Lett. **891**, L1 (2020).
- [35] A. G. Adame, J. Aguilar, S. Ahlen, S. Alam, D. M. Alexander, M. Alvarez, O. Alves, A. Anand, U. Andrade *et al.* (DESI Collaboration), J. Cosmol. Astropart. Phys. 02 (2025) 021.
- [36] T. M. C. Abbott, M. Acevedo, M. Adamow, M. Aguena, A. Alarcon, S. Allam, O. Alves, F. Andrade-Oliveira, J. Annis *et al.* (DES Collaboration), arXiv:2503.06712.
- [37] T. M. C. Abbott, M. Adamow, M. Aguena, S. Allam, O. Alves, A. Amon, F. Andrade-Oliveira, J. Asorey, S. Avila, D. Bacon *et al.*, Phys. Rev. D 110, 063515 (2024).
- [38] T. M. C. Abbott, M. Acevedo, M. Aguena, A. Alarcon, S. Allam, O. Alves, A. Amon, F. Andrade-Oliveira, J. Annis et al. (DES Collaboration), Astrophys. J. Lett. 973, L14 (2024).
- [39] Z. Haiman, J. J. Mohr, and G. P. Holder, Astrophys. J. 553, 545 (2001).
- [40] G. P. Holder, Z. Haiman, and J. J. Mohr, Astrophys. J. Lett. 560, L111 (2001).
- [41] M. Lima and W. Hu, Phys. Rev. D 70, 043504 (2004).
- [42] S. W. Allen, A. E. Evrard, and A. B. Mantz, Annu. Rev. Astron. Astrophys. 49, 409 (2011).

- [43] A. Vikhlinin, A. V. Kravtsov, R. A. Burenin, H. Ebeling, W. R. Forman, A. Hornstrup, C. Jones, S. S. Murray, D. Nagai, H. Quintana *et al.*, Astrophys. J. **692**, 1060 (2009).
- [44] A. B. Mantz, A. von der Linden, S. W. Allen, D. E. Applegate, P. L. Kelly, R. G. Morris, D. A. Rapetti, R. W. Schmidt, S. Adhikari, M. T. Allen *et al.*, Mon. Not. R. Astron. Soc. 446, 2205 (2015).
- [45] C. Garrel, M. Pierre, P. Valageas, D. Eckert, F. Marulli, A. Veropalumbo, F. Pacaud, N. Clerc, M. Sereno, K. Umetsu et al., Astron. Astrophys. 663, A3 (2022).
- [46] I. N. Chiu, M. Klein, J. Mohr, and S. Bocquet, Mon. Not. R. Astron. Soc. 522, 1601 (2023).
- [47] V. Ghirardini, E. Bulbul, E. Artis, N. Clerc, C. Garrel, S. Grandis, M. Kluge, A. Liu, Y. E. Bahar, F. Balzer *et al.*, Astron. Astrophys. **689**, A298 (2024).
- [48] S. Bocquet, J. P. Dietrich, T. Schrabback, L. E. Bleem, M. Klein, S. W. Allen, D. E. Applegate, M. L. N. Ashby, M. Bautz, M. Bayliss *et al.*, Astrophys. J. **878**, 55 (2019).
- [49] S. Bocquet, S. Grandis, L. E. Bleem, M. Klein, J. J. Mohr, T. Schrabback, T. M. C. Abbott, P. A. R. Ade, M. Aguena, A. Alarcon *et al.*, Phys. Rev. D **110**, 083510 (2024).
- [50] S. Bocquet, S. Grandis, E. Krause, C. To, L. E. Bleem, M. Klein, J. J. Mohr, T. Schrabback, A. Alarcon, O. Alves et al., Phys. Rev. D 111, 063533 (2025).
- [51] E. Rozo, R. H. Wechsler, E. S. Rykoff, J. T. Annis, M. R. Becker, A. E. Evrard, J. A. Frieman, S. M. Hansen, J. Hao, D. E. Johnston *et al.*, Astrophys. J. 708, 645 (2010).
- [52] M. Costanzi, E. Rozo, M. Simet, Y. Zhang, A. E. Evrard, A. Mantz, E. S. Rykoff, T. Jeltema, D. Gruen, S. Allen et al., Mon. Not. R. Astron. Soc. 488, 4779 (2019).
- [53] C. To, E. Krause, E. Rozo, H. Wu, D. Gruen, R. H. Wechsler, T. F. Eifler, E. S. Rykoff, M. Costanzi, M. R. Becker *et al.*, Phys. Rev. Lett. **126**, 141301 (2021).
- [54] G. F. Lesci, F. Marulli, L. Moscardini, M. Sereno, A. Veropalumbo, M. Maturi, C. Giocoli, M. Radovich, F. Bellagamba, M. Roncarelli *et al.*, Astron. Astrophys. 659, A88 (2022).
- [55] T. Sunayama, H. Miyatake, S. Sugiyama, S. More, X. Li, R. Dalal, M. M. Rau, J. Shi, I. n. Chiu, M. Shirasaki *et al.*, Phys. Rev. D **110**, 083511 (2024).
- [56] A. Fumagalli, M. Costanzi, A. Saro, T. Castro, and S. Borgani, Astron. Astrophys. 682, A148 (2024).
- [57] T. M. C. Abbott, M. Aguena, A. Alarcon, S. Allam, S. Allen, J. Annis, S. Avila, D. Bacon, K. Bechtol, A. Bermeo *et al.*, Phys. Rev. D **102**, 023509 (2020).
- [58] C.-H. To, E. Krause, E. Rozo, H.-Y. Wu, D. Gruen, J. DeRose, E. Rykoff, R. H. Wechsler, M. Becker, M. Costanzi et al., Mon. Not. R. Astron. Soc. 502, 4093 (2021).
- [59] A. N. Salcedo, H.-Y. Wu, E. Rozo, D. H. Weinberg, C.-H. To, T. Sunayama, and A. Lee, Phys. Rev. Lett. 133, 221002 (2024).
- [60] C.-H. To et al., companion paper, Phys. Rev. D 112, 063537 (2025).
- [61] C.-H. To, J. DeRose, R. H. Wechsler, E. Rykoff, H.-Y. Wu, S. Adhikari, E. Krause, E. Rozo, and D. H. Weinberg, Astrophys. J. 961, 59 (2024).
- [62] E. Krause et al. arXiv:2105.13548.
- [63] J. DeRose, R. H. Wechsler, M. R. Becker *et al.*, Phys. Rev. D **105**, 123520 (2022).

- [64] C.-H. To, E. Rozo, E. Krause, H.-Y. Wu, R. H. Wechsler, and A. N. Salcedo, J. Cosmol. Astropart. Phys. 01 (2023) 016
- [65] M. Costanzi, E. Rozo, E. S. Rykoff, A. Farahi, T. Jeltema, A. E. Evrard, A. Mantz, D. Gruen, R. Mandelbaum, J. DeRose *et al.*, Mon. Not. R. Astron. Soc. 482, 490 (2019).
- [66] Y. Zhang, T. Jeltema, D. L. Hollowood, S. Everett, E. Rozo, A. Farahi, A. Bermeo, S. Bhargava, P. Giles, A. K. Romer et al., Mon. Not. R. Astron. Soc. 487, 2578 (2019).
- [67] J. Myles, D. Gruen, A. B. Mantz, S. W. Allen, R. G. Morris, E. Rykoff, M. Costanzi, C. To, J. DeRose, R. H. Wechsler et al., Mon. Not. R. Astron. Soc. 505, 33 (2021).
- [68] H.-Y. Wu, M. Costanzi, C.-H. To, A. N. Salcedo, D. H. Weinberg, J. Annis, S. Bocquet, M. E. da Silva Pereira, J. DeRose, J. Esteves *et al.*, Mon. Not. R. Astron. Soc. **515**, 4471 (2022).
- [69] Z. Zhang, H.-Y. Wu, Y. Zhang, J. Frieman, C.-H. To, J. DeRose, M. Costanzi, R. H. Wechsler, S. Adhikari, E. Rykoff et al., Mon. Not. R. Astron. Soc. 523, 1994 (2023).
- [70] M. Aguena, O. Alves, J. Annis, D. Bacon, S. Bocquet, D. Brooks, A. Carnero Rosell, C. Chang, M. Costanzi, C. Coviello *et al.*, arXiv:2309.06593.
- [71] P. M. Kelly, J. Jobel, O. Eiger, A. Abd, T. E. Jeltema, P. Giles, D. L. Hollowood, R. D. Wilkinson, D. J. Turner, S. Bhargava *et al.*, Mon. Not. R. Astron. Soc. **533**, 572 (2024).
- [72] C. Zhou, H.-Y. Wu, A. N. Salcedo, S. Grandis, T. Jeltema, A. Leauthaud, M. Costanzi, T. Sunayama, D. H. Weinberg, T. Zhang *et al.*, Phys. Rev. D **110**, 103508 (2024).
- [73] A. Lee, H.-Y. Wu, A. N. Salcedo, T. Sunayama, M. Costanzi, J. Myles, S. Cao, E. Rozo, C.-H. To, D. H. Weinberg *et al.*, Phys. Rev. D 111, 063502 (2025).
- [74] I. Sevilla-Noarbe, K. Bechtol, M. Carrasco Kind, A. Carnero Rosell, M. R. Becker, A. Drlica-Wagner, R. A. Gruendl, E. S. Rykoff, E. Sheldon, B. Yanny *et al.*, Astrophys. J. Suppl. Ser. **254**, 24 (2021).
- [75] I. Sevilla-Noarbe *et al.* (DES Collaboration), Astrophys. J. Suppl. Ser. **254**, 24 (2021).
- [76] B. Abolfathi, D. S. Aguado, G. Aguilar, C. Allende Prieto, A. Almeida, T. T. Ananna, F. Anders, S. F. Anderson, B. H. Andrews, B. Anguiano *et al.*, Astrophys. J. Suppl. Ser. 235, 42 (2018).
- [77] A. Farahi, A. E. Evrard, E. Rozo, E. S. Rykoff, and R. H. Wechsler, Mon. Not. R. Astron. Soc. 460, 3900 (2016).
- [78] M. Costanzi, E. Rozo, M. Simet, Y. Zhang, A. E. Evrard, A. Mantz, E. S. Rykoff, T. Jeltema, D. Gruen, S. Allen et al., Mon. Not. R. Astron. Soc. 488, 4779 (2019).
- [79] T. McClintock, T.N. Varga, D. Gruen, E. Rozo, E.S. Rykoff, T. Shin, P. Melchior, J. DeRose, S. Seitz, J. P. Dietrich et al., Mon. Not. R. Astron. Soc. 482, 1352 (2019).
- [80] J. Tinker, A. V. Kravtsov, A. Klypin, K. Abazajian, M. Warren, G. Yepes, S. Gottlöber, and D. E. Holz, Astrophys. J. 688, 709 (2008).
- [81] E. W. Upsdell, P. A. Giles, A. K. Romer, R. Wilkinson, D. J. Turner, M. Hilton, E. Rykoff, A. Farahi, S. Bhargava, T. Jeltema *et al.*, Mon. Not. R. Astron. Soc. **522**, 5267 (2023).
- [82] S. Grandis, M. Costanzi, J. J. Mohr, L. E. Bleem, H. Y. Wu, M. Aguena, S. Allam, F. Andrade-Oliveira, S. Bocquet, D. Brooks *et al.*, Astron. Astrophys. **700**, A15 (2025).

- [83] E. S. Rykoff, E. Rozo, D. Hollowood, A. Bermeo-Hernandez, T. Jeltema, J. Mayers, A. K. Romer, P. Rooney, A. Saro, C. Vergara Cervantes *et al.*, Astrophys. J. Suppl. Ser. **224**, 1 (2016).
- [84] E. S. Sheldon and E. M. Huff, Astrophys. J. **841**, 24 (2017).
- [85] M. Gatti, S. Pandey, E. Baxter, J. C. Hill, E. Moser, M. Raveri, X. Fang, J. DeRose, G. Giannini, C. Doux *et al.*, Phys. Rev. D **105**, 123525 (2022).
- [86] J. Myles, A. Alarcon *et al.* (DES Collaboration), Mon. Not. R. Astron. Soc. **505**, 4249 (2021).
- [87] M. Gatti, G. Giannini *et al.* (DES Collaboration), Mon. Not. R. Astron. Soc. **510**, 1223 (2022).
- [88] N. MacCrann *et al.* (DES Collaboration), Mon. Not. R. Astron. Soc. **509**, 3371 (2022).
- [89] A. Porredon *et al.* (DES Collaboration), Phys. Rev. D 103, 043503 (2021).
- [90] M. Rodríguez-Monroy et al., Mon. Not. R. Astron. Soc. 511, 2665 (2022).
- [91] J. De Vicente, E. Sánchez, and I. Sevilla-Noarbe, Mon. Not. R. Astron. Soc. 459, 3078 (2016).
- [92] M. Jarvis, TreeCorr: Two-point correlation functions, Astrophysics Source Code Library, record ascl:1508.007 (2015).
- [93] DES Collaboration, Dark energy survey year 6 results: Multi-probe modeling strategy and validation.
- [94] J. A. Blazek, N. MacCrann, M. A. Troxel, and X. Fang, Phys. Rev. D 100, 103506 (2019).
- [95] Y. Park, E. Rozo, and E. Krause, Phys. Rev. Lett. 126, 021301 (2021).

- [96] A. J. Mead, S. Brieden, T. Tröster, and C. Heymans, Mon. Not. R. Astron. Soc. 502, 1401 (2021).
- [97] S. Pandey et al., Phys. Rev. D 106, 043520 (2022).
- [98] S. Grandis, V. Ghirardini, S. Bocquet, C. Garrel, J. J. Mohr, A. Liu, M. Kluge, L. Kimmig, T. H. Reiprich, A. Alarcon et al., Astron. Astrophys. 687, A178 (2024).
- [99] C. Doux et al. (DES Collaboration), Mon. Not. R. Astron. Soc. 503, 2688 (2021).
- [100] F. Kleinebreil, S. Grandis, T. Schrabback, V. Ghirardini, I.-N. Chiu, A. Liu, M. Kluge, T. H. Reiprich, E. Artis, E. Bahar *et al.*, Astron. Astrophys. **695**, A216 (2025).
- [101] M. Raveri and C. Doux, Phys. Rev. D **104**, 043504 (2021).
- [102] X. T. Tang, D. Brout, T. Karwal, C. Chang, V. Miranda, and M. Vincenzi, Astrophys. J. Lett. 983, L27 (2025).
- [103] https://des.ncsa.illinois.edu/releases/y3a2/Y3key-cluster.
- [104] J. McCullough, A. Amon, E. Legnani, D. Gruen, A. Roodman, O. Friedrich, N. MacCrann, M. R. Becker, J. Myles, S. Dodelson *et al.*, arXiv:2410.22272.
- [105] E. Krause, X. Fang, S. Pandey, L. F. Secco, O. Alves, H. Huang, J. Blazek, J. Prat, J. Zuntz, T. F. Eifler et al., arXiv:2105.13548.
- [106] L. E. Bleem, M. Klein, T. M. C. Abbot, P. A. R. Ade, M. Aguena, O. Alves, A. J. Anderson, F. Andrade-Oliveira, B. Ansarinejad, M. Archipley *et al.*, Open J. Astrophys. 7, 13 (2024).
- [107] B. Diemer, Astrophys. J. Suppl. Ser. 239, 35 (2018).
- [108] B. Diemer and M. Joyce, Astrophys. J. 871, 168 (2019).
- [109] M. Costanzi, A. Saro, S. Bocquet, T. M. C. Abbott, M. Aguena, S. Allam, A. Amara, J. Annis, S. Avila, D. Bacon et al., Phys. Rev. D 103, 043522 (2021).